

## Constraining Nuclear Molecular Gas Content with High-resolution CO Imaging of GOALS Galaxies

JAMES AGOSTINO,<sup>1</sup> ANNE M. MEDLING,<sup>1</sup> LORETO BARCOS-MUÑOZ,<sup>2,3</sup> VIVIAN U,<sup>4</sup>  
 MYNOR RODRÍGUEZ VÁSQUEZ,<sup>5</sup> GEORGE C. PRIVON,<sup>6,7,8</sup> CLAUDIA CICONE,<sup>9</sup> LEE ARMUS,<sup>10</sup>  
 JORGE MORENO,<sup>11,12</sup> CLAUDIO RICCI,<sup>13,14</sup> YIQING SONG,<sup>15,16</sup> CHRISTOPHER C. HAYWARD,<sup>17,18,19</sup>  
 KATHERINE ALATALO,<sup>20,21</sup> AND DAVID B. SANDERS<sup>22</sup>

<sup>1</sup>*Ritter Astrophysical Research Center and Department of Physics & Astronomy, University of Toledo, Toledo, OH 43606, USA*

<sup>2</sup>*National Radio Astronomy Observatory, 520 Edgemont Road, Charlottesville, VA, 22903, USA*

<sup>3</sup>*Department of Astronomy, University of Virginia, 530 McCormick Road, Charlottesville, VA, 22903, USA*

<sup>4</sup>*4129 Frederick Reines Hall, Department of Physics and Astronomy, University of California, Irvine, CA 92697, USA*

<sup>5</sup>*Instituto de Investigación en Ciencias Físicas y Matemáticas USAC, Ciudad Universitaria, Zona 12, 01012, Guatemala, Guatemala*

<sup>6</sup>*National Radio Astronomy Observatory, 520 Edgemont Road, Charlottesville, VA 22903*

<sup>7</sup>*Department of Astronomy, University of Florida, P.O. Box 112055, Gainesville, FL 32611, USA*

<sup>8</sup>*Department of Astronomy, University of Virginia, 530 McCormick Road, Charlottesville, VA 22904, USA*

<sup>9</sup>*Institute of Theoretical Astrophysics, University of Oslo, PO Box 1029, Blindern, 0315 Oslo, Norway*

<sup>10</sup>*IPAC, California Institute of Technology, 1200 East California Boulevard, Pasadena, CA 91125, USA*

<sup>11</sup>*Department of Physics and Astronomy, Pomona College, Claremont, CA 91711, USA*

<sup>12</sup>*The Observatories of the Carnegie Institution for Science, 813 Santa Barbara Street, Pasadena, CA 91101, USA*

<sup>13</sup>*Instituto de Estudios Astrofísicos, Facultad de Ingeniería y Ciencias, Universidad Diego Portales, Avenida Ejercito Libertador 441, Santiago, Chile*

<sup>14</sup>*Kavli Institute for Astronomy and Astrophysics, Peking University, Beijing 100871, China*

<sup>15</sup>*European Southern Observatory, Alonso de Córdova, 3107, Vitacura, Santiago, 763-0355, Chile*

<sup>16</sup>*Joint ALMA Observatory, Alonso de Córdova, 3107, Vitacura, Santiago, 763-0355, Chile*

<sup>17</sup>*Eureka Scientific, Inc., 2452 Delmer Street, Suite 100, Oakland, CA 94602, USA*

<sup>18</sup>*Kavli Institute for the Physics and Mathematics of the Universe (WPI), The University of Tokyo Institutes for Advanced Study, The University of Tokyo, Kashiwa, Chiba 277-8583, Japan*

<sup>19</sup>*Center for Computational Astrophysics, Flatiron Institute, 162 Fifth Avenue, New York, NY 10010, USA*

<sup>20</sup>*Space Telescope Science Institute, 3700 San Martin Drive, Baltimore, MD 21211, USA*

<sup>21</sup>*William H. Miller III Department of Physics and Astronomy, Johns Hopkins University, Baltimore, MD 21218, USA*

<sup>22</sup>*Institute for Astronomy, University of Hawaii, 2680 Woodlawn Drive, Honolulu, HI 96822*

### ABSTRACT

We present measurements of the cool molecular gas mass around the nuclei of two gas-rich mergers, III Zw 035 and IRAS F01364–1042, whose enclosed masses ( $M_{\text{enc}}$ ) within the central 40–80 pc would be overmassive if attributed entirely to the supermassive black hole mass (SMBH) and compared to SMBH-galaxy scaling relations. Our gas mass measurements are derived from Atacama Large Millimeter/submillimeter Array (ALMA) Band 6 long-baseline observations of CO(J=2-1) and 230 GHz continuum emission at 14–20 pc resolution, which probes below the resolving limit of the previous black hole mass measurements. Subtracting molecular gas mass from these enclosed

masses is not enough to reconcile with BH-galaxy relationships, but independently measuring  $M_{\text{enc}}$  using the cold CO(2-1) gas does shift the black holes down to their expected values. Still, these ALMA data reveal respective molecular gas masses of  $\sim 3 \times 10^7$  to  $\sim 6 \times 10^8 M_{\odot}$  within 70 pc of these black holes, which could challenge some black hole accretion models that assume nuclear gas like this has no angular momentum.

## 1. INTRODUCTION

Every massive galaxy in our universe is thought to host a supermassive black hole (SMBH) in its center. These SMBHs typically contain masses millions or billions times the mass of our Sun. Their gravitational sphere of influence is tiny (of order  $\sim 1\text{-}100$  pc, the radius of which can be defined as  $r_{\text{SOI}} \approx GM_{\text{BH}}/\sigma_*^2$ ; see [Yoon 2017](#)) when compared to the typical kpc to hundreds of kpc scale sizes of galaxies. Despite this, a number of galaxy-wide properties correlate with the mass of the central SMBH. These are the so-called black hole mass ( $M_{\text{BH}}$ ) scaling relations, where SMBH mass scales with host galaxy properties like bulge luminosity ([Kormendy 1993](#); [Ho 1999](#); [Marconi & Hunt 2003](#); [McConnell & Ma 2013](#)), stellar mass ([Silk & Rees 1998](#); [Magorrian et al. 1998](#); [Kormendy & Gebhardt 2001](#); [McLure & Dunlop 2002](#); [Häring & Rix 2004](#); [Bennert et al. 2011](#); [Cisternas et al. 2011](#)), and bulge velocity dispersion ([Gebhardt et al. 2000](#); [Merritt & Ferrarese 2001](#); [Tremaine et al. 2002](#); [Gültekin et al. 2009](#); [Beifiori et al. 2012](#); [McConnell & Ma 2013](#)). The mechanism driving these relations is not well understood and the search for a physically-motivated picture for the co-evolution is an active area of research (see [Kormendy & Ho 2013](#) and [Heckman & Best 2014](#) for reviews and [Bennert et al. 2021](#) for a recent study on local galaxies).

One of the major uncertainties in placing galaxies on the SMBH-galaxy scaling relations is a precise measurement of the  $M_{\text{BH}}$ . Even with very-long-baseline interferometry, the region near the event horizon can only be directly “observed” around the nearest, most massive SMBHs ([Event Horizon Telescope Collabora-](#)

[tion et al. 2019](#)). Depending on the target and data available, multiple approaches can be taken to measure SMBH mass. Some of these methods include reverberation mapping ([Clavel et al. 1991](#); [Horne et al. 2004](#); [Vestergaard & Peterson 2006a](#); [Cackett et al. 2021](#)), Schwarzschild modeling ([Schwarzschild 1979](#); [Faber & Jackson 1976](#); [Lauer et al. 1995](#); [Kormendy et al. 1997](#); [Cretton et al. 1999](#); [Gebhardt et al. 2000](#); [van den Bosch et al. 2008](#); [Walsh et al. 2012](#)), direct measurements of stellar orbits ([Ghez et al. 2008](#); [Genzel et al. 2010](#)), dynamical modeling of stars and gas in circum-nuclear disks ( $>1$  pc) ([Cappellari 2008](#); [Barth et al. 2009](#); [Medling et al. 2011](#); [U et al. 2013](#); [Medling et al. 2014](#)), and empirically-calibrated proxies (e.g. [Vestergaard & Peterson 2006b](#); [Morgan et al. 2010](#); [Bentz et al. 2013](#); [U et al. 2022](#)).

In this paper, we refer to a parent sample of nine SMBH masses within gas rich mergers derived via gas and stellar kinematics in [Medling et al. \(2015\)](#). These enclosed mass ( $M_{\text{enc}}$ , mass under  $r = 77$  mas from the SMBH) measurements use data from Keck/OSIRIS adaptive optics (AO) and target galaxies from the Great Observatory All-sky LIRG Survey (GOALS, [Armus et al. 2009](#)). In the K-band, these data use the CO (2-0) and (3-1) bandheads to trace kinematics of young stars along with emission from  $\text{Br}\gamma$  and  $\text{H}_2$ . LIRGs (luminous infrared galaxies) emit an excess of light in the infrared ( $L_{\text{IR}} > 10^{11} L_{\odot}$  by definition; [Sanders & Mirabel 1996](#)) powered by vigorous activity from either star formation or AGN, or both. Based on the dynamical ( $M_{\text{enc}}$ ) measurements in [Medling et al. \(2015\)](#), individual galaxies like III Zw 035

and IRAS F01364–1042 are significantly offset (by between  $\sim 0.5$  -  $2.5$  dex) from the canonical black hole mass scaling relations: supermassive black hole mass ( $M_{\text{BH}}$ ) vs. stellar velocity dispersion ( $\sigma_*$ ), total stellar mass ( $M_*$ ), and bulge luminosity ( $L_{\text{H, bulge}}$ ). Non-LIRG spiral galaxies do not typically lie above scaling relations (Davis et al. 2018; Davis et al. 2019), and whether most LIRGs do remains in question. Overmassive black holes present a challenge to the canonical understanding of gas-rich mergers, which predicts that these black holes will grow more in an upcoming quasar phase — placing them in even greater conflict with scaling relations (Mirabel & Sanders 1988; Hopkins et al. 2008b; Hopkins et al. 2008a).

The results from Medling et al. (2015) were surprising but came with a caveat: the resolution of the Keck/OSIRIS+AO data does not probe all the way down to the expected SMBH  $r_{\text{SOI}} \approx 10$  pc (or less; value estimated for IRAS F01364–1042 based on  $\sigma_*$  found in Medling et al. 2015 and equation 3 of Kormendy & Ho 2013). Those dynamically-derived SMBH mass measurements in Medling et al. (2015) are a  $M_{\text{enc}}$  within the highest achievable resolution by OSIRIS at a 35 mas plate scale, 77 mas (a Nyquist sampling rate of 2.2; see Medling et al. 2019), meaning they could include significant extended stellar and gaseous mass. This paper is focused on quantifying exactly how much molecular gas mass exists within that limit, then completing an independent  $M_{\text{enc}}$  measurement for comparison. Medling et al. (2019) performed a pilot study focused on measuring molecular gas mass in one of these galaxies that host double nuclei, NGC 6240. Using Atacama Millimeter/submillimeter Array (ALMA) Band 6 CO( $J=2-1$ ) and continuum data to measure molecular gas mass, they found that in the northern nucleus, the black hole shifts down to scaling relations after the gas mass correction, as up to 89% of the previously measured en-

closed mass could be attributed to gas rather than the black hole. In contrast, the dynamical mass of the southern nucleus consists of up to only 11% gas mass, leaving it above scaling relations. The following work estimates the amount of molecular gas mass in two other gas-rich, merging LIRGs with the purpose of understanding whether or not these galaxies host overmassive black holes. Such confirmation would be further evidence for an accretion paradigm in which the SMBH grows before the global galaxy properties in scaling relations, which is contrary to the timeline of accretion in typical systems (Hopkins 2012; Cen 2012; Anglés-Alcázar et al. 2017).

In this Paper we determine whether the amount of gas present within the resolving limit of the original dynamical mass measurements accounts for the observed disagreement with scaling relations. We then measure an independent  $M_{\text{enc}}$  using the CO(2-1) kinematics. This paper is structured as follows. Section 2 details the CO(2-1) measurements obtained from the ALMA and how the imaging process of these measurements was conducted. Section 4 explains how we calculated molecular gas mass estimates via both CO(2-1) and ALMA Band 6 continuum. Section 5 describes independent  $M_{\text{enc}}$  measurements using the same CO(2-1) cubes and how they compare to the Medling et al. (2015)  $M_{\text{enc}}$ . Section 6 contextualizes these results within the picture of scaling relations and what those results mean for our current picture of the co-evolution of merging gas-rich galaxies and their SMBHs.

The two galaxy merger systems featured in this paper are III Zw 035 and IRAS F01364–1042. III Zw 035 is at  $z = 0.02744$  and R.A. = 01h44m30.50s, dec. = +17d06m05.0s with a total infrared luminosity  $\log(L_{\text{IR}}/L_{\odot}) = 11.64$ . IRAS F01364–1042 is at  $z = 0.04823$  and R.A. = 01h38m52.921s, dec. = -10d27m11.42s with a total infrared luminosity  $\log(L_{\text{IR}}/L_{\odot}) =$

11.85 (Armus et al. 2009). If III Zw 035 or IRAS F01364–1042 host AGNs, they must be dust-obscured.

In this work, we use cosmological parameters of  $H_0 = 70 \text{ km s}^{-1} \text{ Mpc}^{-1}$ ,  $\Omega_m = 0.28$ , and  $\Omega_\Lambda = 0.72$  (Hinshaw et al. 2009). To calculate spatial scales and luminosity distances for III Zw 035 and IRAS F01364–1042 we use Ned Wright’s Cosmology Calculator (Wright 2006). III Zw 035 has a scale of  $554 \text{ pc arcsec}^{-1}$  and IRAS F01364–1042 has a scale of  $1012 \text{ pc arcsec}^{-1}$ .

## 2. MEASUREMENTS AND IMAGING

The nuclei of III Zw 035 and IRAS F01364–1042 were observed with Keck-OSIRIS+AO in 2010 and 2011 (Medling et al. 2014). This integral field spectroscopy was used to measure dynamical masses at a resolution of 77 mas (Medling et al. 2015). As our science goal is to resolve the inner-most molecular gas in these galactic nuclei, our Band 6 observations were taken in ALMA’s second-most extended configuration, C43-9 (PI Medling, project codes 2018.1.01123.S and 2019.1.00811.S). In these programs, there is also  $\sim 0.14''$  resolution imaging in Band 6, which we do not use because we prioritize the highest angular resolution imaging. III Zw 035 was observed twice on 2019 June 20th (maximum recoverable scale [MRS] =  $0.4''$ ) and once 2021 August 21 (MRS =  $0.6''$ ) for a total of 6649 s on source. IRAS F01364–1042 was observed on 2021 August 30 (MRS =  $0.5''$ ) and on 2021 August 8 in the C43-8 configuration (MRS =  $0.8''$ ) and for a total of 3160 s on source. For all measurement sets we follow the standard calibration pipeline and manually examined each measurement set to make sure flagging was complete. Then, for IRAS F01364–1042 we concatenated both measurement sets, checking for any inconsistencies in the relative weightings of each configuration. Compared to only using the configuration 9 measurement set, the combined measurement sets give an rms that is a fac-

tor of  $\sim \sqrt{2}$  lower and improves our signal by approximately the same value because of the increased effective exposure time and uv-sampling of the slightly more compact C43-8 configuration. Next, we imaged the line-free channels to produce continuum maps for each galaxy. This included avoiding not only the CO(2-1) line in both galaxies, but also lines like CS(5-4) and HC<sub>3</sub>N which are prominent in the core of III Zw 035. We then perform continuum subtraction in the uv-plane and image the spectral window containing CO, producing a spectral cube for each galaxy. After imaging with Briggs weighting (Briggs 1995; `robust` =  $-0.5$ ), our achieved (averaged) synthesized beam resolutions (FWHMs) for the data sets used in our analysis for IRAS F01364–1042 and III Zw 035 respectively, are 41 and 30 mas for the spectral cubes and 29 and 26 mas for the continuum images. All of these data are firmly under the resolution used in the prior dynamical measurements. For III Zw 035, we achieved a rms of  $1.11 \text{ mJy beam}^{-1}$  in a channel width,  $\Delta v$ , of  $10.4 \text{ km s}^{-1}$  and a continuum rms of  $0.033 \text{ mJy beam}^{-1}$  while for IRAS F01364–1042 we achieved a rms of  $0.43 \text{ mJy beam}^{-1}$  in a channel width,  $\Delta v$ , of  $11.2 \text{ km s}^{-1}$  and a continuum rms of  $0.029 \text{ mJy beam}^{-1}$ . Table 1 lists relevant properties of these measurement sets and Figure 1 shows Hubble I-Band images (GO-10592; PI: Evans) of both of III Zw 035 and IRAS F01364–1042 overlaid with ALMA Band 6 CO(2-1) contours. These contours were made using CO(2-1) imaged at a slightly lower resolution (`robust` =  $0.5$ ) than the dataset we use for our analysis.

We use the Common Astronomy Software Applications (*CASA*, CASA Team et al. 2022) package developed by the NRAO, ESO, and NAOJ to do this imaging. `tclean`, a routine within *CASA*, takes the measured visibilities and reconstructs a sky model. One of the `tclean` parameters that is part of the Briggs weighting scheme (Briggs 1995), `robust`, ad-

justs how different parts of the uv-plane (in Fourier space) are weighted. To test the impact of the `robust` parameter on our results, we performed our analysis on a range of values ( $-0.5, 0, 0.5, 2$ ). For our galaxies using a `robust` parameter of  $-0.5$  recovers 90% of the flux compared to the default pipeline value of (0.5) and provides the benefit of producing an image with a narrower beam FWHM.

Achieving the highest available spatial resolution matches our science goal by probing gas mass as close to the black hole as possible and so we chose `robust = -0.5` as our default imaging for the analysis in this paper (both for CO and continuum).

### 3. MORPHOLOGY

#### 3.1. *III Zw 035*

As defined by the merger classification from [Stierwalt et al. \(2013\)](#) in optical wavelengths, III Zw 035 is a pre-merger. This means that this galaxy and its companion have not yet had their first encounter. Figure 2 shows ALMA Band 6 CO, and continuum, along with a moment 1 (velocity) map of CO(2-1) for III Zw 035 and IRAS F01364–1042. The high resolution  $\sim 26$  mas molecular gas emission in III Zw 035 reveals a resolved core in CO with a peak integrated intensity that is slightly offset (5–10 pc) from the center of Band 6’s continuum emission ( $\sim 230$  GHz). Continuum contours highlight several resolved clumpy substructures about 20–30 pc away from the central CO source. Previously, [Pihlström et al. \(2001\)](#) found clumps of OH maser and 18 cm continuum emission in similar positions around the central source. Further inspection of the ALMA data cubes in these clumps shows the presence of CS(5-4), a good dense gas tracer ([Wang et al. 2011](#)). The clumpy nature of this dense gas tracer and evidence from previous observations could indicate that there are star-forming clumps around III Zw 035’s core. These clumps may also be

part of a forming or otherwise evolving torus or ring around III Zw 035’s nucleus, as distances of the clumps to the core are typical (10s of pc) for these sorts of structures (e.g. [García-Burillo et al. 2021](#)). CO(2-1) is not apparent in all of these clumps. Additional matched resolution data at other wavelengths, such as deeper ALMA Band 7 and Band 3 continuum, are necessary to further constrain the nature of this distribution of mass.

The CO moment 1 maps (Figure 2, bottom left) show strong disk-like rotation across the major axis of the galaxy, similar to what is seen in H<sub>2</sub> and Br $\gamma$  ([Medling et al. 2014](#)). III Zw 035 also shows evidence of a molecular outflow along the minor axis seen in the H<sub>2</sub> and Br $\gamma$  maps in [U et al. \(2019\)](#), as well as in CO(1-0) at lower resolution in [Lutz et al. \(2020\)](#). III Zw 035’s outflow can also be seen in CO(2-1) and it will be discussed in detail in a future work.

#### 3.2. *IRAS F01364-1042*

Toward the opposite end of the merger spectrum, IRAS F01364–1042 is classified as a late-stage merger in [Stierwalt et al. \(2013\)](#). The two galaxies have their nuclei in the same envelope at the center of the system. As seen in Figure 2, compared to III Zw 035, the brightest CO(2-1) emission in IRAS F01364–1042 has an edge-on disk-like morphology that traces the continuum emission well, with a central source that seems to be marginally resolved. Similar to III Zw 035, it shows disk-like rotation in the high-resolution CO(2-1) imaging, with symmetrical velocity gradients on either side of the disk that match well to the H<sub>2</sub> and Pa $\alpha$  maps at  $\sim 2$ – $3 \times$  coarser resolution in [Medling et al. \(2014\)](#). The CO(2-1) data presented in this work show evidence of the presence of an outflow, along the minor axis, originating from the nucleus. This outflow is also supported by MIRI H<sub>2</sub> and ALMA CO(1-0) maps (Song et al. in review).

### 4. COMPUTING NUCLEAR GAS MASS

Galaxy	$D_L$ (Mpc)	Merger Stage	ALMA Band	Resolution (pc)	Freq. (GHz)	CO Flux (Jy km s <sup>-1</sup> )	Cont. Flux (mJy)
III Zw 035	110	Pre-Merger	3	59.53	106.88	4.61	3.67
			6	13.62	224.38	1.61	5.04
IRAS F01364–1042	209.9	Late-Stage	3	97.15	104.79	2.33	2.98
			6	19.23	219.84	8.79	2.80

**Table 1.** List of galaxy and observational properties used in this work. All data were taken in the long baseline ALMA 12m configuration. The frequency column shows the observed CO(1-0) and CO(2-1) frequencies. The merger stage definitions are from [Stierwalt et al. \(2013\)](#) where pre-merger is defined as galaxies prior to their first encounter and late-stage describes two nuclei in a common envelope (but that still show signs of a merger). Fluxes listed are integrated flux within the 77 mas aperture used throughout this work. Absolute flux uncertainties in ALMA Band 3 and Band 6 data are 5 and 10%, respectively ([Cortes et al. 2023](#)).

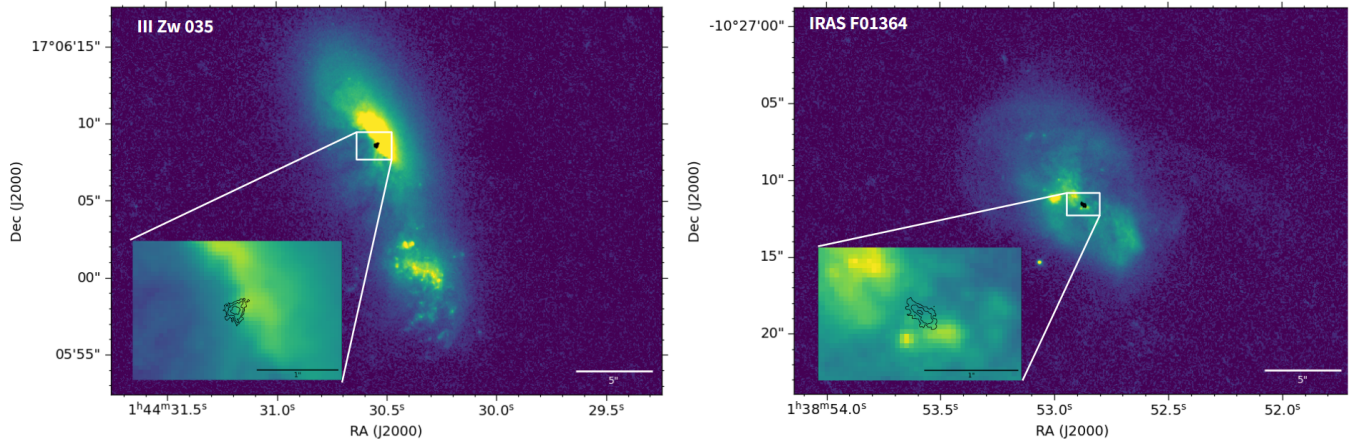


**Figure 1.** I-Band Hubble ACS images (GO-10592; PI: Evans) of III Zw 035 (left) and IRAS F01364–1042 (right) with CO(2-1) moment 0 contours overlaid in black. Moment 0 contours are from  $10^{-0.4}$  to  $10^{0.5}$  Jy beam<sup>-1</sup> km s<sup>-1</sup> for III Zw 035 and  $10^{-0.8}$  to  $10^{0.5}$  Jy beam<sup>-1</sup> km s<sup>-1</sup> for IRAS F01364–1042 in 7 logarithmically-spaced intervals. III Zw 035’s companion galaxy still retains much of its large-scale structure, while in IRAS F01364–1042 the two are in a later stage of the merger process.

Our goal in this work is to calculate the amount of the nuclear molecular gas mass that falls within the resolution limit of Keck-OSIRIS+AO ( $\sim 77$  mas). Following [Medling et al. \(2019\)](#), in this section we describe our two main methods of calculating molecular gas mass. Additionally, we perform independent enclosed mass estimates for comparison to [Medling et al. \(2015\)](#) through position-velocity (PV) diagrams in Section 5. We summarize and comment on the results of these analyses in Section 6.

As in [Medling et al. \(2019\)](#), we measure nuclear gas masses to compare with  $M_{\text{enc}}$  derived from stellar and gas kinematics from [Medling et al. \(2015\)](#). We include these original BH masses for III Zw 035 and IRAS F01364–1042 in the top row of Table 2. In this study we do not include comparisons to III Zw 035’s enclosed warm gas mass because of high uncertainties attributed to the H<sub>2</sub> and Br $\gamma$  outflow seen along its minor axis [U et al. \(2019\)](#). For IRAS F01364–1042, we use the  $M_{\text{enc}}$  derived via gas kinematics, which could be impacted by

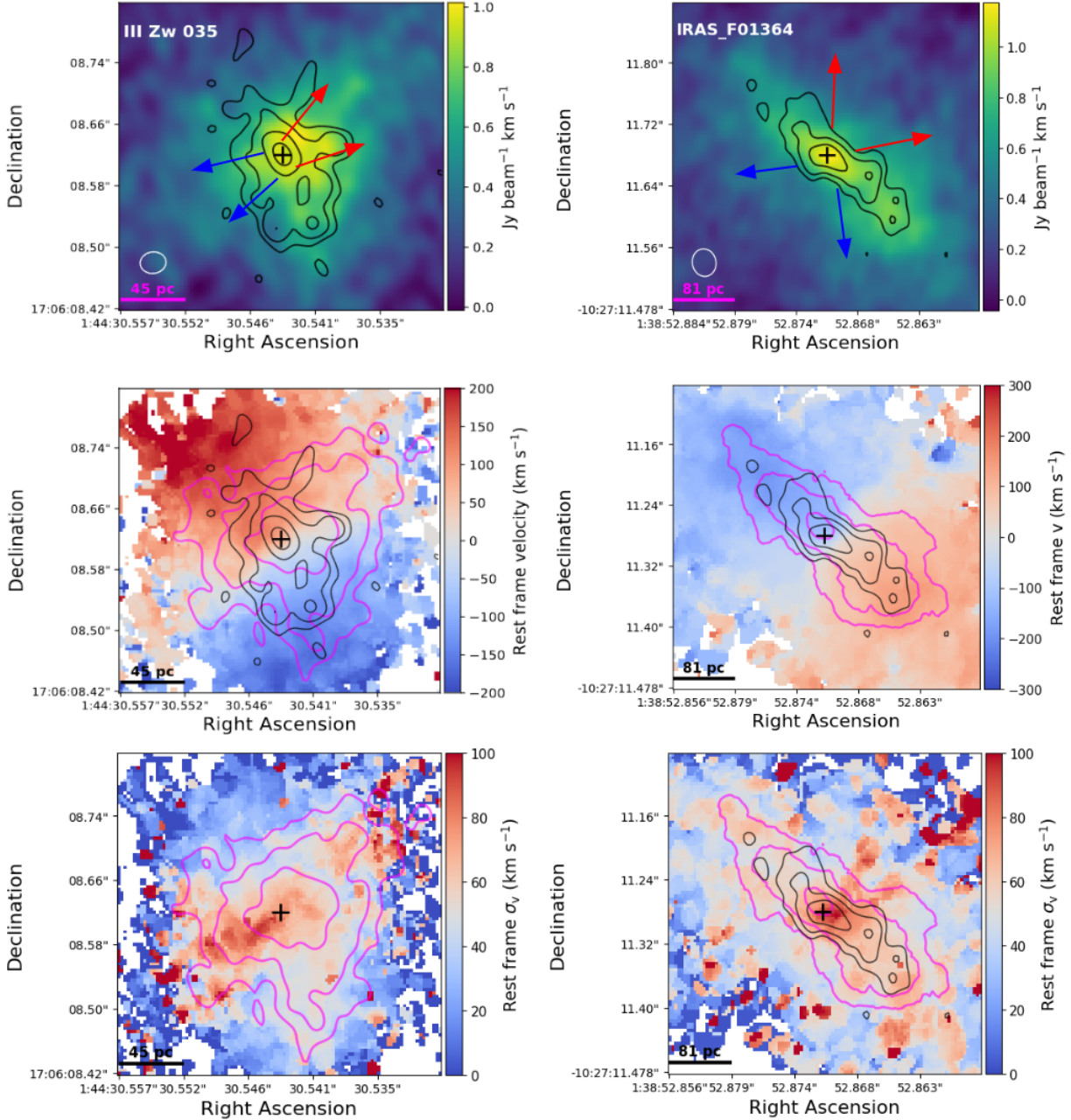


**Figure 2.** *Top:* CO(2-1) moment 0 (integrated intensity) maps for III Zw 035 (left) and IRAS F01364–1042 (right) with Band 6 continuum contours at 230 GHz for III Zw 035 and 228 GHz for IRAS F01364–1042 with levels at 3, 6, 12, 24, 48  $\times$  (rms) Jy beam $^{-1}$  (rms values are  $32.7 \times$  and  $29.4 \times \mu\text{Jy beam}^{-1}$  for III Zw 035 and IRAS F01364–1042 respectively). White ellipses indicate the beam sizes of the CO images ( $33 \times 28$  for III Zw 035 and  $43 \times 40$  mas for IRAS F01364–1042). *Bottom; Middle:* CO(2-1) moments 1 (velocity) and 2 (velocity dispersion) maps. Black contours are the same as in the top two panels for continuum, while magenta contours are moment 0 contours from  $10^{-0.4}$  to  $10^{0.5}$  Jy beam $^{-1}$  km s $^{-1}$  for III Zw 035 and  $10^{-0.8}$  to  $10^{0.5}$  Jy beam $^{-1}$  km s $^{-1}$  for IRAS F01364–1042 in 7 logarithmically-spaced intervals. Velocity maps for both galaxies are clipped to a  $3\sigma$  CO(2-1) detection. Continuum center, where we expect the black hole to be located, is indicated by a black cross. Red and blue arrows indicate the directionality (red and blue-shifts relative to the galaxy's systemic velocity) of the molecular outflows.

the potential outflowing component; however, no stellar dynamics-based mass is available.

#### 4.1. Gas mass via CO(2-1)

While H<sub>2</sub> is an abundant interstellar gas, its net-zero dipole moment makes carbon monoxide a commonly used tracer molecule for cold H<sub>2</sub> (Solomon et al. 1972; Wilson et al. 1974; Scoville & Solomon 1975; Burton et al. 1975). To calculate a molecular gas mass from our spectral cube we start with the full, 1.875 GHz wide cube, then, in python, integrate across the channels with CO emission in each pixel. To determine if a channel has CO emission in it, we use a combination of visual inspection of the individual channel maps and integrated spectra in a rectangular region made in *CASA*. This produces a moment 0, or flux map of CO(2-1). Then, to include broader spatial integration regions we step outward in a box shape for CO-detected pixels. Each radial step expands the box in two pixels in each x( $\pm 1$ ) and y( $\pm 1$ ) direction. The same radial stepping method is used in Section 4.2. To convert to mass we must first translate the CO line flux to CO line luminosity  $L'_{\text{CO}(2-1)}$ . For this we apply the equation from Solomon & Vanden Bout (2005):

$$L'_{\text{CO}(2-1)} = (3.25 \times 10^7) S_{\text{CO}} \Delta v (\nu_{\text{obs}}^{-2} D_L^2 (1+z)^{-3}) \text{ K km s}^{-1} \text{ pc}^2 \quad (1)$$

where  $S_{\text{CO}} \Delta v$  is the flux of the CO(2-1) emission (in Jy km s<sup>-1</sup>),  $\nu_{\text{obs}}$  is the observed frequency (in GHz), and  $D_L$  is the luminosity distance (in Mpc).

To convert from this line luminosity to mass we use the conversion factor  $\alpha_{\text{CO}}$ . The use of low-J CO lines as tracers of molecular gas has been explored for decades;  $\alpha_{\text{CO}}$  or similar conversion factors have been calibrated for both the Milky Way and other galaxies (e.g. as reviewed by Dickman 1978, Combes 1991, and Bolatto et al. 2013). This conversion factor varies depending on where it is being applied, and the

inclination angle of the galaxy. For example, on  $>600$  pc scales, Sandstrom et al. (2013) find mean  $\alpha_{\text{CO}(1-0)}$  values ranging from 2.9 to 8.2. In NGC 3351, using  $\sim 100$  pc resolution ALMA data, Teng et al. (2022) find intensity-weighted values between 1.11 and 1.79 on 2 kpc scale, and find that the conversion factor is lower in inflow regions. Medling et al. (2019) used an  $\alpha_{\text{CO}(2-1)}$  conversion factor calibrated spatially by Cicone et al. (2018) for the nuclear regions of NGC 6240. NGC 6240 is a local, merging LIRG like our systems, but it does host X-ray detected AGN and a clear double nucleus, unlike our systems.

In this work, as in Medling et al. (2019), we use the  $\alpha_{\text{CO}(1-0)} = 2.3 \pm 1.2$  which is derived from the central box ‘C1’ of NGC 6240 and provided by C. Cicone via private communication following the methods in Cicone et al. (2018). We scale this  $\alpha_{\text{CO}(1-0)}$  to  $\alpha_{\text{CO}(2-1)}$  by independently measuring  $r_{21}$  ( $r_{21} = L'_{\text{CO}(2-1)} / L'_{\text{CO}(1-0)}$ ) at 100 mas resolution in both III Zw 035 and IRAS F01364–1042 (57 and 98 pc, respectively). To measure this new  $r_{21}$  we created beam-matched images by first smoothing the CO(2-1) data to the CO(1-0) data (project code 2017.1.01235.S; PI: Barcos-Muñoz) by using *CASA*’s **imsmooth** task, which performs a Fourier-based convolution to the CO(1-0) beam in which we used a Gaussian kernel. We then used the smoothed image to measure the line luminosities in the same  $154 \times 154$  mas box used in our analysis. The new  $\alpha_{\text{CO}(2-1)}$  value (which includes both H<sub>2</sub> and helium) for III Zw 035 is calculated as:

$$\alpha_{\text{CO}(2-1)} = \frac{\alpha_{\text{CO}(1-0)}}{r_{21}} = \frac{2.3 \pm 1.2}{0.88 \pm 0.099} = 2.60 \pm 1.2 \text{ M}_\odot (\text{K km s}^{-1} \text{ pc}^2)^{-1}. \quad (2)$$

and the same calculations are done for IRAS F01364–1042 which has a  $r_{21} = 0.77 \pm 0.086$  and  $\alpha_{\text{CO}(2-1)} = 3.0 \pm 1.2 \text{ M}_\odot (\text{K km s}^{-1} \text{ pc}^2)^{-1}$ . Uncertainties on  $r_{21}$  are the result of error prop-

agation of the ALMA Band 3 and 6 flux uncertainties of 5 and 10%, respectively (Diaz Trigo et al. 2019). Using these  $\alpha_{\text{CO}(2-1)}$  estimates rather than adopting the value from Ciccone et al. (2018) increases the final gas ( $\text{H}_2$  and helium) mass calculated in III Zw 035 and IRAS F01364–1042 by factors of 1.1 and 1.3, respectively.

Montoya Arroyave et al. (2023) measure a median  $\alpha_{\text{CO}(1-0)} = 1.7 \pm 0.5 \text{ M}_\odot$  in 37 ULIRGs (ultra-luminous infrared galaxies,  $L_{\text{IR}} > 10^{12} \text{ L}_\odot$ ) and 3 LIRGs (see also Herrero-Illana et al. 2019). Sandstrom et al. (2013) found that in the central kpc of 26 starburst galaxies,  $\alpha_{\text{CO}(1-0)}$  is a factor of  $\sim 2$  smaller than in the larger scale disk. Each of these studies found median  $\alpha_{\text{CO}(1-0)}$  values lower than the typical global value for the Milky Way ( $4.4 \text{ M}_\odot (\text{K km s}^{-1} \text{ pc}^2)^{-1}$ ; Bolatto et al. 2013). These measurements were done on larger scales than the ones we make our  $M_{\text{enc}}$  measurements in, but suggest that globally-calibrated  $\alpha_{\text{CO}(1-0)}$  values cannot be trusted for analysis on nuclear scales. The  $\alpha_{\text{CO}(2-1)}$  we adopt here is therefore uncertain particularly compared to larger scale estimates of  $\alpha_{\text{CO}(1-0)}$ , because of the lack of studies which robustly calibrate these nuclear conversion factors on  $< 50$  pc scales in LIRGs. In this work we attempt to mitigate for these uncertainties by using the highest resolution calibrated  $\alpha_{\text{CO}(1-0)}$  from Ciccone et al. (2018) for NGC 6240, a merging (U)LIRG.

The CO(2-1) flux profiles, which are multiplied by  $\alpha_{\text{CO}(2-1)}$  to obtain a mass profile, are shown in the top two rows of Figure 3. Inside the 77 mas Keck-OSIRIS resolution limit achieved in Medling et al. (2015) we find  $(3.6 \pm 1.9) \times 10^7 \text{ M}_\odot$  of molecular gas mass for III Zw 035 and  $(6.7 \pm 2.8) \times 10^8 \text{ M}_\odot$  of molecular gas mass for IRAS F01364–1042 within 43.7 and 76.9 pc, respectively. Fractionally these values account for between  $\sim 1$  and  $\sim 48\%$  (including

$1\sigma$  errors) of the previously determined  $M_{\text{enc}}$  (see Table 2 for details).

#### 4.2. Gas mass via dust continuum

Another way of estimating the central molecular gas mass is by measuring the cospatial dust mass using our mm-wavelength continuum imaging. For LIRGs, the mm/sub-mm continuum flux densities are typically dominated by thermal dust emission (U et al. 2012). Continuum measurements start with the same aperture as in Section 4.1 (a  $154 \times 154$  mas square), integrating flux density as the box grows outward. We then use the calibrated dust continuum flux density ratio to  $\text{H}_2$  from Scoville et al. (2016). This calibration improves on the Scoville et al. (2015) relation used for Arp 220, but it assumes a globally-derived, mass weighted dust temperature ( $T_D$ ) of 25 K. In the sample of ULIRGs from U et al. (2012), the average global  $T_D$  was found to be moderate at  $\sim 25\text{--}45$  K. Other recent studies have shown that luminosity-weighted nuclear  $T_D$  can be much higher than this (e.g. Sakamoto et al. 2021), and so we explore a range of temperatures from 100–500 K for our primary analysis.

As our continuum-based measurements use a relation that assumes the emission is from dust, for them to be accurate we have to ensure that any contaminants to that emission are removed. Some of the continuum flux density at  $\sim 230$  GHz may be due to synchrotron radiation (originating from buried AGN and/or supernova remnants) and free-free emission (Condon & Ransom 2016). We can predict the contributions of these phenomena to our continuum flux by utilizing previous observations of our galaxies at lower frequencies where synchrotron and free-free emission dominate the flux, extrapolating their spectra to our frequencies. To estimate the contribution of synchrotron and free-free emission to our measured continuum flux, we use 32.5 GHz integrated fluxes from Very Large Array observations found in

Barcos-Muñoz et al. (2017). Together with integrated ALMA Band 3 observations (project 2017.1.01235.S, PI Barcos-Muñoz, see Table 1), we can measure the spectral index of both synchrotron and free-free contributions together between 32.5 and  $\sim$ 100 GHz, then extrapolate the 32.5 GHz flux to ALMA Band 6 using that spectral index. For III Zw 035 the spectral index  $\alpha = -0.58 \pm 0.04$  and for IRAS F01364–1042  $\alpha = -0.39 \pm 0.04$ . Uncertainties are calculated as a combination of image noise and errors in calibration flux uncertainties for ALMA and the VLA (Diaz Trigo et al. 2019; Partridge et al. 2016).

To estimate the contribution of these contaminants to the Band 6 continuum, we use the  $\sim$ 120 mas resolution, 32.5 GHz VLA data from Barcos-Muñoz et al. (2017) and the spectral indices mentioned prior. We extrapolate the 32.5 GHz integrated flux to a Band 6 flux density value using:

$$f_{\text{extra}} = f_{\text{synch}} + f_{\text{free-free}} = f_{32.5\text{GHz}} \left( \frac{\nu_{\text{cont}}}{32.5\text{GHz}} \right)^\alpha \quad (3)$$

where  $\nu_{\text{cont}}$  is the center of the continuum band for each galaxy in GHz, and the flux densities (f) are in Jy. The resulting contributions to our continuum flux by both synchrotron and free-free sources are 43% and 70% for III Zw 035 and IRAS F01364–1042, respectively.

These contributions are subtracted in the following equation, which adopts a modified blackbody spectral index  $\beta = 1.8$ , where we perform our gas mass conversion (Equation 3; Scoville et al. 2015):

$$\frac{0.868 \times (f_{\text{cont}} - f_{\text{extra}}) D_L^2}{(1+z)^{4.8} T_{25} \nu_{350}^{3.8} \Gamma_{RJ} 10^3 \text{Mpc}} 10^{10} M_\odot \quad (4)$$

where the fluxes ( $f_{\text{cont}}$  is continuum flux density) are in mJy, luminosity distance,  $D_L$ , is in Mpc,  $T$  is normalized to 25 K,  $\nu$  normalized to

350 GHz, and  $\Gamma_{RJ}$  is the correction for departure in the rest frame of the Planck function from Rayleigh-Jeans, which varies with temperature (Scoville et al. 2016).

Using two bracketing dust temperature cases, 100 K and 500 K, we find gas masses inside the 77 mas Keck-OSIRIS resolution (box) limit of  $(9.8 \pm 0.43) \times 10^7 M_\odot$  to  $(5.1 \pm 0.22) \times 10^8 M_\odot$  of mass for III Zw 035 and  $(1.2 \pm 0.50) \times 10^8 M_\odot$  to  $(6.4 \pm 2.6) \times 10^8 M_\odot$  of mass for IRAS F01364–1042 within 43.7 and 76.9 pc, respectively. Rows 3 and 4 of Figure 3 show the continuum flux density and molecular gas masses as a function of radius. Fractionally, in relation to the previously determined  $M_{\text{enc}}$  from Medling et al. (2015), these measured values account for as little as  $\sim$ 5% in the high  $T_D$  case to as much as  $\sim$ 75% in the low temperature case (see Table 2 for details). This wide range of gas masses and the topic of dust temperature are discussed within Section 6.2.

### 4.3. Spectral index mapping

To better understand the nature of the mm continuum emission in the nuclei of our galaxies, we create inter-band spectral index maps. To create such maps for our galaxies, we generate line-free continuum images for Band 3 (project 2017.1.01235.S, PI Barcos-Muñoz) and Band 6 (data presented here) with the same pixel and beam sizes and using a **robust** =  $-0.5$ . We then compute the spectral index per pixel defined as:

$$\alpha = \log\left(\frac{f_{\text{B6}}}{f_{\text{B3}}}\right) / \log\left(\frac{\nu_{\text{B6}}}{\nu_{\text{B3}}}\right) \quad (5)$$

where  $f$  is the flux density in Jy and  $\nu$  is the frequency (in GHz). B3 and B6 indicate the values of flux density and frequency of the images mentioned above. Data below a  $3 \times \text{rms}$  threshold is masked and not mapped. As a general rule, a positive mm spectral index favors dust emission (Planck Collaboration et al. 2016), while a steep negative mm spectral index indicates dominant

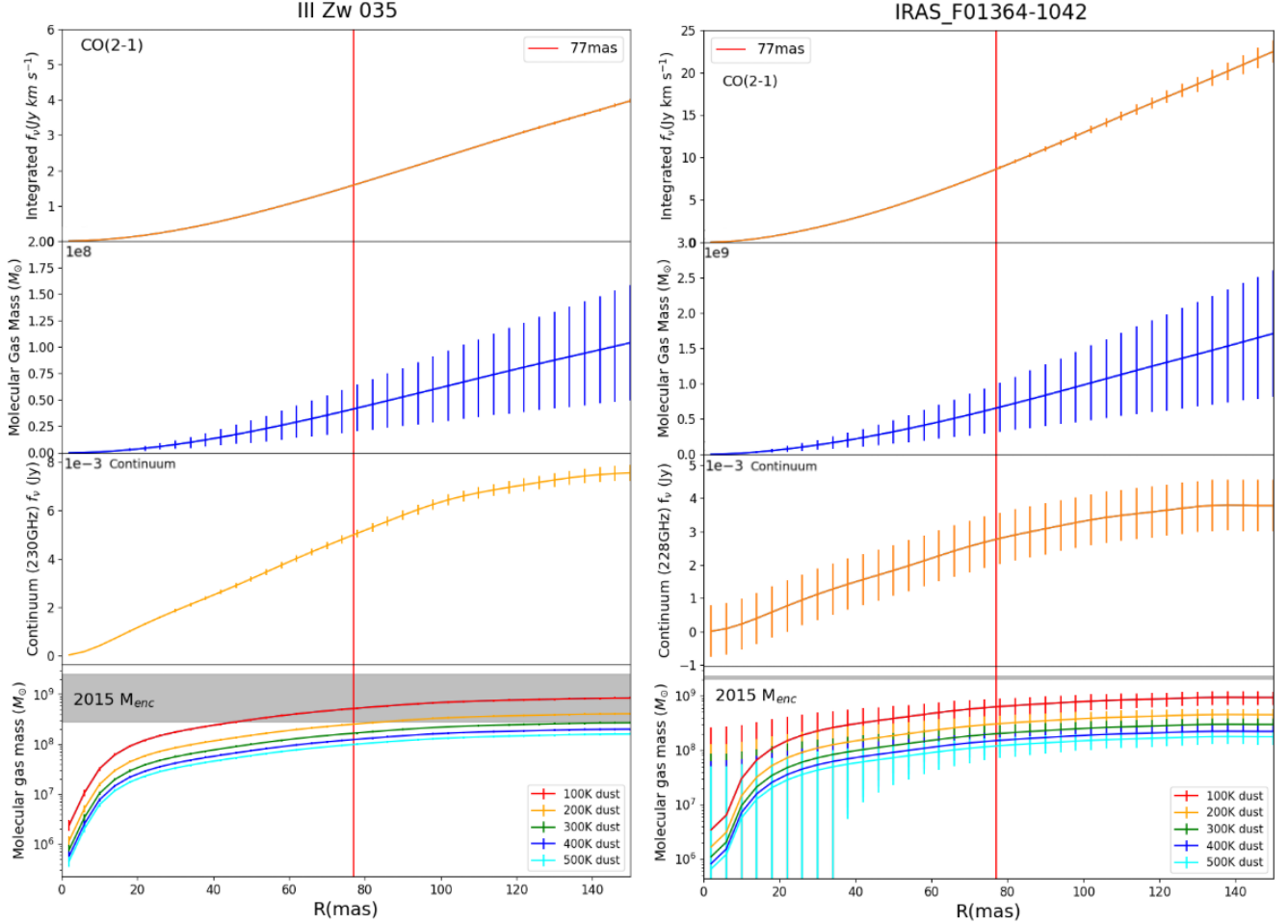


**Figure 3.** Integrated measurements and calculated masses within the boxed aperture for IRAS F01364–1042 and III Zw 035. *First row:* enclosed CO(2-1) flux from images described in Section 2. *Second row:*  $M_{\text{enc}}$  calculated from CO(2-1) fluxes shown in above panels using method described in Section 4.1. *Third row:* integrated continuum flux densities at 230 GHz (III Zw 035) and 228 GHz (IRAS F01364–1042) extracted from images described in Section 2. *Bottom row:*  $M_{\text{enc}}$  calculated from continuum fluxes shown in above panels using method described in Section 4.2. Grey regions are Medling et al. (2015)  $M_{\text{enc}}$  ranges. III Zw 035 requires a  $T_D \gtrsim 175$  K to have a dust-derived gas mass lower than the previous  $M_{\text{enc}}$  while IRAS F01364–1042 requires a  $T_D \gtrsim 19$  K.

synchrotron emission (see Section 4.2). We estimated the uncertainty of the spectral index via error propagation considering the uncertainty in the flux density due to noise in the image and the ALMA flux calibration uncertainties.

In Figure 4, we show the spectral index maps and related error maps for both galaxies. Given the resolution restrictions of our spectral index maps, we don't have independent measurements of the spectral indices of the nuclei versus the clumpy torus-like structures in III Zw

035. The integrated interband (Band 3 to 6) spectral index values for III Zw 035 and IRAS F01364–1042, respectively, are  $0.87 \pm 0.31$  and  $0.49 \pm 0.27$ . Alongside the  $f_{\text{extra}}$  measurements in Section 4.2 that estimate contribution fractions of free-free and synchrotron emission of  $<50\%$ , these spectral index maps suggest that thermal dust emission is a major contributor to the Band 6 continuum emission over other non-thermal or free-free contributions. Further observations at matched resolution to the Band

Integrated gas masses compared to previous  $M_{\text{enc}}$  measurements

		III Zw 035	IRAS F01364–1042
<sup>(1)</sup> $M_{\text{enc}}$	Gas ( $\text{H}_2$ , $\text{Br}\gamma$ )	*	$(2.2^{+0.60}_{-0.17}) \times 10^9 M_{\odot}$
	Stellar (disk)	$(>6.8^{+1.0}_{-4.0}) \times 10^8 M_{\odot}$	-
	Stellar (JAM)	$(<2.0^{+5.0}_{-0.70}) \times 10^9 M_{\odot}$	-
<sup>(2)</sup> $M_{\text{gas,CO}}$		$(3.6 \pm 1.9) \times 10^7 M_{\odot}$	$(6.7 \pm 2.8) \times 10^8 M_{\odot}$
<sup>(4)</sup> Gas fraction		$<5.3^{+0.95\%}_{-1.4\%}$	$30^{+18\%}_{-18\%}$
		$>1.8^{+1.0\%}_{-1.1\%}$	
<sup>(3)</sup> $M_{\text{gas,cont}(100\text{K})}$		$(5.1 \pm 0.22) \times 10^8 M_{\odot}$	$(6.4 \pm 2.6) \times 10^8 M_{\odot}$
<sup>(4)</sup> Gas fraction		$>26^{+9.0\%}_{-6.5\%}$	$28^{+12\%}_{-12\%}$
		$<75^{+44\%}_{-3.4\%}$	
<sup>(3)</sup> $M_{\text{gas,cont}(500\text{K})}$		$(9.8 \pm 0.43) \times 10^7 M_{\odot}$	$(1.2 \pm 0.50) \times 10^8 M_{\odot}$
<sup>(4)</sup> Gas fraction		$>4.9^{+1.2\%}_{-1.7\%}$	$5.4^{+2.2\%}_{-2.3\%}$
		$<14^{+8.5\%}_{-0.7\%}$	

**Table 2.** Summary of results for mass estimates via CO ( $\alpha_{\text{CO}}$  method) and thermal dust continuum. For III Zw 035 we compare to  $M_{\text{enc}}$  from stellar kinematics and in IRAS F01364–1042 we compare to  $M_{\text{enc}}$  from gas kinematics. \*III Zw 035 gas-based dynamical masses exist in [Medling et al. \(2015\)](#), but we do not use them for comparison in this work due to likely contamination from a molecular outflow. (1):  $M_{\text{enc}}$  from [Medling et al. \(2015\)](#). (2): Gas mass from CO(2-1) flux as calculated in Section 4.1. (3): Gas mass from thermal excess continuum flux as calculated in Section 4.2. (4): Percentages displayed are relative to the kinematically-derived  $M_{\text{enc}}$  found in [Medling et al. \(2015\)](#) and are computed as  $M_{\text{gas}}/M_{\text{enc}}$ .

6 data are necessary to learn more about the radio SEDs of these cores and clumps to make a more direct comparison to our other results.

## 5. INDEPENDENT ENCLOSED MASS MEASUREMENTS

The results in Section 4 present corrected [Medling et al. \(2015\)](#)  $M_{\text{BH}}$  values for III Zw 035 and IRAS F01364–1042. With those corrections, the black holes remain overmassive except in the case of III Zw 035 with  $T_D \lesssim 175$  K. In this subsection, we independently measure  $M_{\text{enc}}$  at the Band 6 beam resolution using the CO cubes presented in this work.

### 5.1. *Tilted-ring modeling*

To calculate dynamical  $M_{\text{enc}}$  we model the CO kinematics using the tilted-ring modeling algorithm <sup>3D</sup>Barolo ([Di Teodoro & Fraternali 2015](#)). Using our high resolution CO(2-1) cubes, <sup>3D</sup>Barolo models tilted rings with inclination-

corrected rotational velocities to the line emission at a range of distances from the center. This 3D modeling approach is preferred over a 2D method in large part due to the instrumental effect of beam smearing being accounted for during the convolution step ([Di Teodoro & Fraternali 2015](#)). We provide initial guesses to <sup>3D</sup>Barolo’s two-stage 3DFIT task for parameters like inclination, PA, and redshift. We tested different methods of building the <sup>3D</sup>Barolo mask as well, using both SEARCH and SMOOTH&SEARCH. Models and residuals produced in this way are shown in Appendix A. In III Zw 035, the outflow likely dominates the velocity dispersion map. Position angles modeled by <sup>3D</sup>Barolo are about 15 degrees lower than those in [Medling et al. \(2014\)](#). This difference in PA may be due to the modeling in this work using kinematics of the cold gas rather than warm gas.

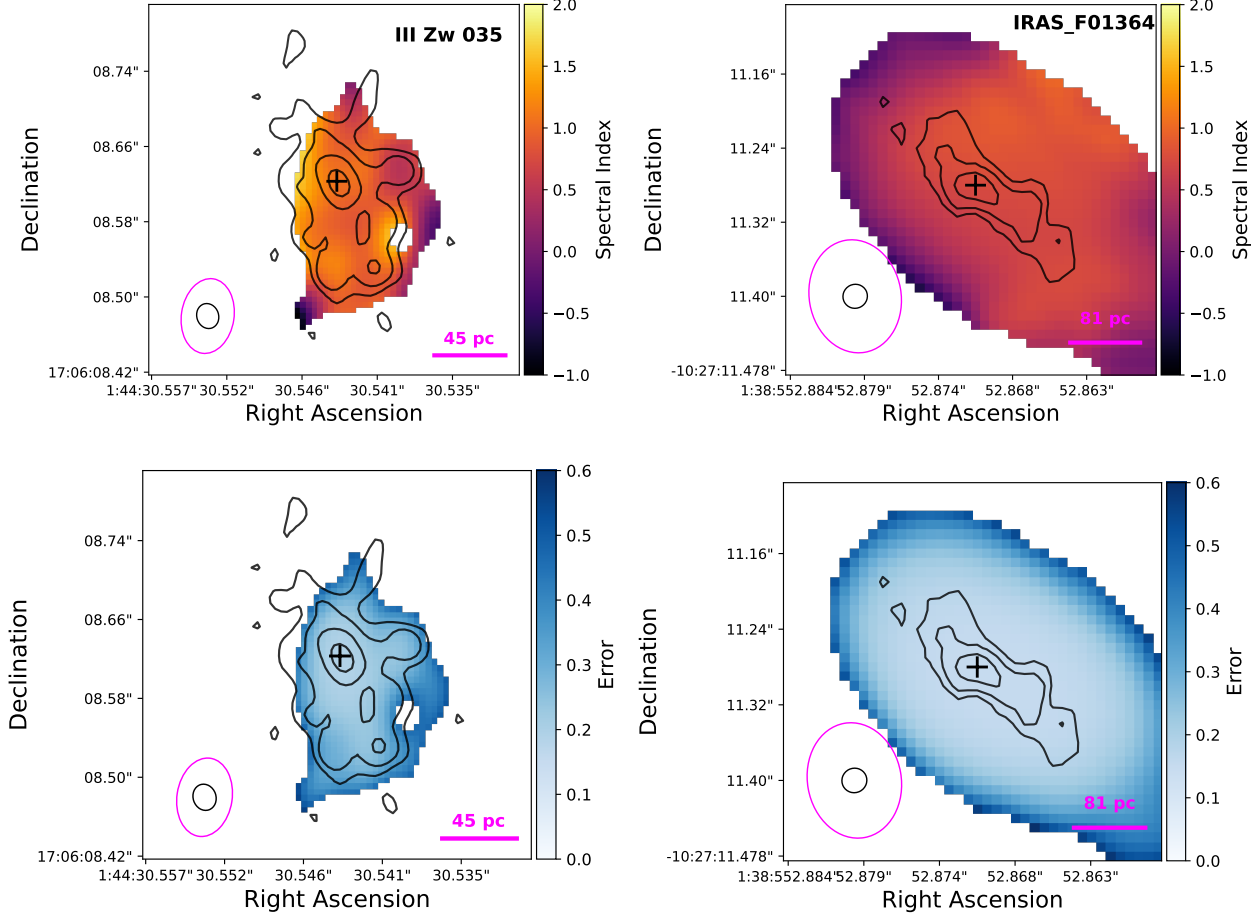


**Figure 4.** Spectral index (top) and uncertainty maps (bottom) for III Zw 035 (left) and IRAS F01364–1042 (right). The beam sizes of the continuum images used to create the spectral index maps ( $0.075'' \times 0.052''$  for III Zw 035 and  $0.134'' \times 0.110''$  for IRAS F01364–1042) are shown in the lower left corners in magenta. The black contours correspond to the Band 6 combined line-free continuum emission at 230 GHz for III Zw 035 and 228 GHz for IRAS F01364–1042 with levels at  $3, 6, 12, 24, 48 \times (\text{rms}) \text{ Jy beam}^{-1}$  (rms values are  $32.9$  and  $38.3 \mu\text{Jy}$  for III Zw 035 and IRAS F01364–1042 respectively). Their beam sizes are shown in the lower left corners in black ( $31 \times 25 \text{ mas}$  for III Zw 035 and  $29 \times 28 \text{ mas}$  for IRAS F01364–1042).

We then use the inclination-corrected, circular velocities  $v$  at radii  $R$  of the kinematic models computed by <sup>3D</sup>Barolo in our  $M_{\text{enc}}$  calculation,  $M_{\text{enc}}(R) = v^2 R G^{-1}$ . This method assumes a spherical mass distribution. The  $M_{\text{enc}}$  profiles, along with the position-velocity models from <sup>3D</sup>Barolo and contours of position-velocity diagrams manually made in CARTA (Cube Analysis and Rendering Tool for Astronomy, Comrie et al. 2021), can be seen in Figure 5.

## 5.2. Comparison to warm gas $M_{\text{enc}}$

At 30 and 39 mas for III Zw 035 and IRAS F01364–1042 respectively, we find  $M_{\text{enc}}$  of  $(5.26_{-2.10}^{+2.21}) \times 10^7$  and  $(2.09_{-0.63}^{+0.52}) \times 10^8 M_{\odot}$  (see Table 2) which are between 91–93% lower than those found in Medling et al. (2015) at 77 mas resolution. In Table 3, we show new upper limits for the central  $M_{\text{BH}}$  by subtracting matched-resolution molecular gas masses from those high-resolution  $M_{\text{enc}}$ . Corrected  $M_{\text{BH}}$  are also compared to BH-galaxy scaling relations in Figure 6.

The first main difference that may be leading to different  $M_{\text{enc}}$  results between the mod-

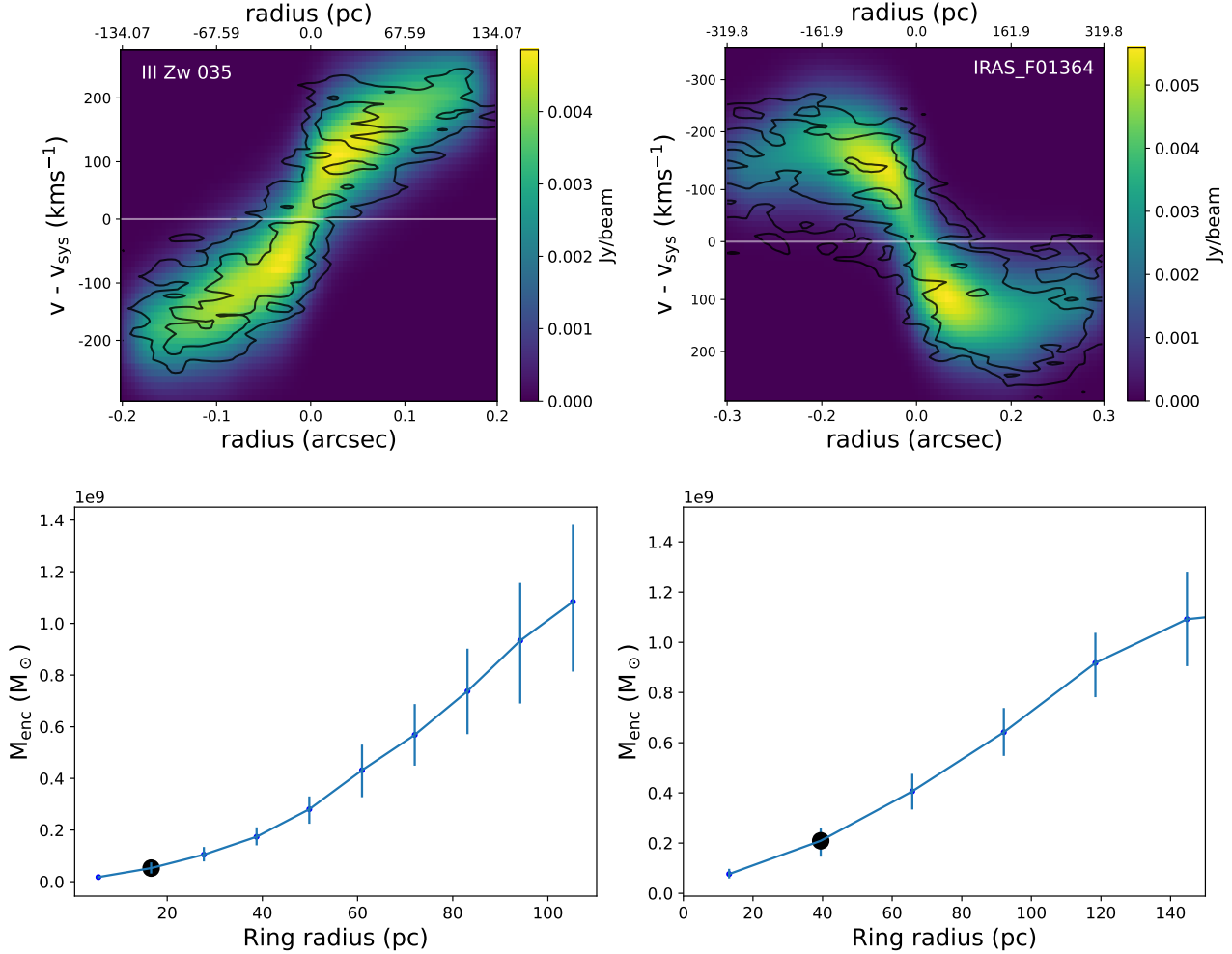


**Figure 5.** Position-velocity (PV) diagrams of the CO emission modeled across the major axis in III Zw 035 (left) & IRAS F01364–1042 (right). *Top:* PV models from <sup>3D</sup>Barolo outputs. Black contours correspond to 3, 6, 9, and 12  $\times$  rms of high resolution PV diagrams made in CARTA at the same central position with the same high resolution input cubes described in Section 2. The white, horizontal lines represent velocities of zero with respect to systematic. *Bottom:* Inclination-corrected  $M_{\text{enc}}$  calculated using the methods described in Section 5.  $M_{\text{enc}}$  was calculated on tilted rings that were separated by single beam widths. Both  $M_{\text{enc}}$  values (measured at radii of a single beam FWHM indicated by the black circles) are about an order of magnitude lower than the measurements made in Medling et al. (2015).

eling here and in Medling et al. (2015) is the nature of the kinematic tracer. In this work, we use CO(2-1), which traces the cold gas in the nuclei of these galaxies while for IRAS F01364–1042 Medling et al. (2015) modeled the warm-gas tracer Pa $\alpha$ . Given the indication of outflows present in IRAS F01364–1042, Pa $\alpha$  may be an unreliable tracer of the bulk motion of the gas (e.g. in Davies et al. 2024). In III Zw 035, although Medling et al. (2015)

derived their masses from stars, which should not be impacted by outflows, the resolution of our cold gas dynamics is higher than obtained with Keck/OSIRIS. The CO beam sizes are 1.5–2 times smaller than the Keck/OSIRIS PSF. This means that we are physically probing kinematics closer to the black hole, thus presumably including less mass other than the black hole (stars, dust, gas) in the process.

Integrated gas masses compared to  $M_{\text{enc}}$  measured in this work

	III Zw 035	IRAS F01364–1042
<sup>(1)</sup> $M_{\text{enc,CO}}$	$(5.3^{+2.2}_{-2.1}) \times 10^7 M_{\odot}$	$(2.1^{+0.52}_{-0.63}) \times 10^8 M_{\odot}$
<sup>(2)</sup> $M_{\text{gas,CO}}$	$(8.6 \pm 4.1) \times 10^6 M_{\odot}$	$(2.4 \pm 1.0) \times 10^8 M_{\odot}$
<sup>(4)</sup> Gas fraction	$16^{+10\%}_{-10\%}$	$110^{+56\%}_{-59\%}$
<sup>(3)</sup> $M_{\text{gas,cont}(100\text{K})}$	$(1.9 \pm 0.98) \times 10^8 M_{\odot}$	$(3.2 \pm 2.6) \times 10^8 M_{\odot}$
<sup>(4)</sup> Gas fraction	$370^{+160\%}_{-150\%}$	$150^{+130\%}_{-130\%}$
<sup>(3)</sup> $M_{\text{gas,cont}(500\text{K})}$	$(3.7 \pm 0.19) \times 10^7 M_{\odot}$	$(6.2 \pm 5.0) \times 10^7 M_{\odot}$
<sup>(4)</sup> Gas fraction	$70^{+30\%}_{-28\%}$	$29^{+25\%}_{-26\%}$

**Table 3.** Summary of results for mass estimates via CO ( $\alpha_{\text{CO}}$  method) and thermal dust continuum when subtracted from  $M_{\text{enc}}$  calculated in this work (see Section 5). All values in this table are measured at a radius equal to the beam size of the respective CO data. (1):  $M_{\text{enc}}$  derived using CO(2-1) kinematics in Section 5. (2): Gas mass from CO(2-1) flux as calculated in Section 4.1. (3): Gas mass from continuum thermal excess flux as calculated in Section 4.2. (4): Percentages displayed are relative to  $M_{\text{enc}}$  derived from CO kinematics and are calculated as  $M_{\text{gas}}/M_{\text{enc,CO}}$ .

The  $M_{\text{enc}}$  presented in this work have the benefits of using a tracer of the dynamically cold gas and physically probing closer to the SMBH than the measurements of Medling et al. (2015). Like the Medling et al. (2015) warm gas and stellar measurements though, for the purpose of comparison to scaling relations, these are still measurements of enclosed mass (from which we can subtract gas mass) rather than  $M_{\text{BH}}$ .

## 6. DISCUSSION

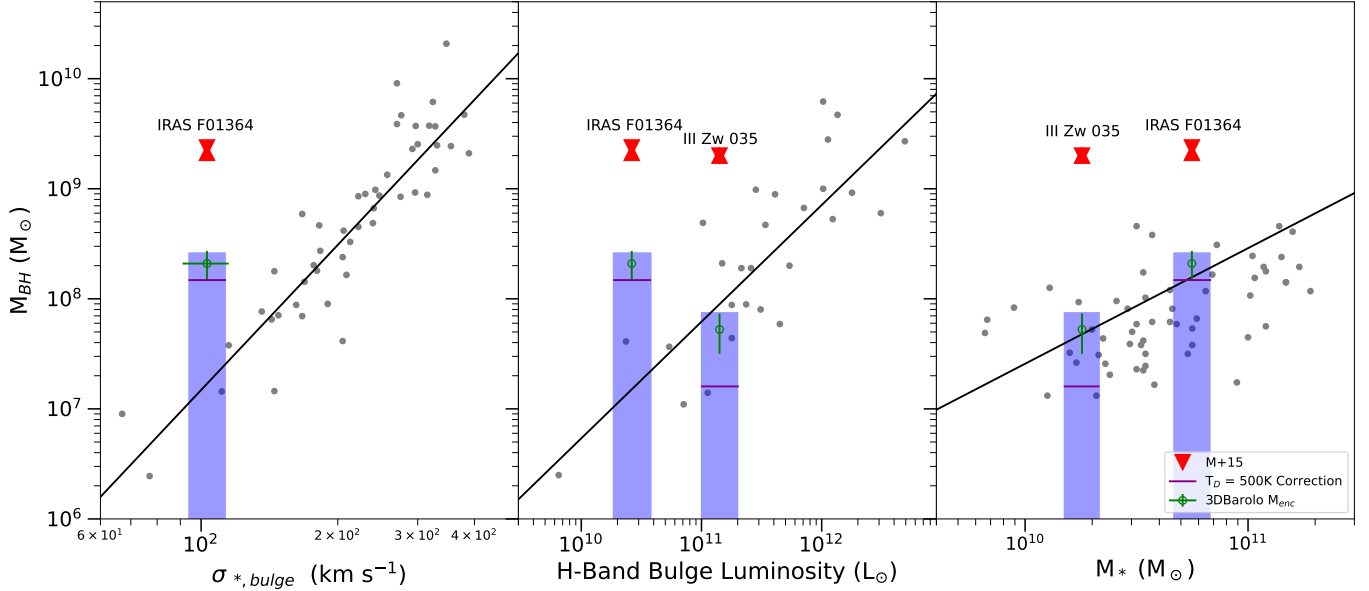
### 6.1. Black hole masses in context

Figure 6 shows the black hole masses with our calculated nuclear gas contaminations removed on three scaling relations:  $M_{\text{BH}}$  vs.  $\sigma_{\star}$ , bulge luminosity  $L_{\text{bulge}}$ , and total stellar mass  $M_{\star}$ . For  $M_{\text{BH}}$  vs.  $\sigma_{\star}$  we use dynamical data on elliptical and classical bulge galaxies compiled in Kormendy & Ho (2013) with their equation 7 for the best-fit line. For  $M_{\text{BH}}$  vs.  $L_{\text{bulge}}$  we use luminosities from Marconi & Hunt (2003) and updated  $M_{\text{BH}}$  from McConnell & Ma (2013) with an updated fit used in Medling et al. (2019). For  $M_{\text{BH}}$  vs. total stellar mass  $M_{\star}$  we use data from Bennert et al. (2011) and Cisternas et al. (2011), along with a best-fit line from McConnell & Ma (2013).

Results depend on the initial  $M_{\text{enc}}$  value used for these two nuclei. If we assume that the Medling et al. (2015)  $M_{\text{enc}}$  (at coarser resolution) is realistic, then the only case where we find enough molecular gas mass to shift either nucleus' dynamically-derived  $M_{\text{BH}}$  down to scaling relations is where III Zw 035's dust temperature  $T_D \lesssim 175$  K.

On the other hand, if we assume the dynamical modeling from Section 5 is better constrained, we find nearly the opposite. In all cases, subtracting the central molecular gas from the dynamical  $M_{\text{enc}}$  causes these black holes to fall on to scaling relations.

This dramatic distinction between the two methods could be caused by several factors. As is posited in Medling et al. (2015), non-circular motion could have an impact on those original BH mass measurements. Warm gas is more likely to trace the turbulent outflow than cold gas, which may have driven up the  $M_{\text{enc}}$  from warm gas. We find evidence for outflowing components along the minor axis in III Zw 035 and IRAS F01364–1042 in CO(2-1) at these small spatial scales. We also find evidence for mild disk warping in both III Zw 035 and IRAS F01364–1042 in CO(2-1) moment maps, al-



**Figure 6.** Medling et al. (2015) (red) and Section 5 (green)  $M_{\text{enc}}$  plotted on black hole scaling relations:  $M_{\text{BH}}$  vs.  $\sigma_*$  (left), bulge luminosity  $L_{\text{bulge}}$  (middle), and total stellar mass  $M_*$  (right). Grey points and line fits are based on various literature measurements, see Section 6.1 for details. Blue shaded regions represent the widest range of molecular gas-corrected  $M_{\text{BH}}$  ( $M_{\text{enc}} - M_{\text{gas}}$ ) where  $M_{\text{enc}}$  is the value computed in this work (see Section 5). Both the CO-derived gas value and the  $T_D = 100\text{--}500$  K continuum methods are included in this range. The purple horizontal lines are the continuum-corrected values with  $T_D = 500$  K. In all cases, the enclosed gas mass corrects the total enclosed mass measured in this work down to (or below) scaling relations.

though primarily beyond the radius used to calculate  $M_{\text{enc}}$ . The disk warping properties on the smallest scales remain unknown, and incorporating corrections for these kinematic deviations – especially for strong central inclination angle shifts – could revise both of the  $M_{\text{enc}}$  measurements. Future work focused on these galaxies will provide additional information on the magnitude of the non-circular motions caused by the outflows, which we can use to constrain their impact on these  $M_{\text{enc}}$  measurements (Song et al. in review for IRAS F01364–1042).

## 6.2. Uncertain Dust Temperature

For our two galaxies, as with the gas, we do not have an accurate estimate for the dust temperature on the scales studied in this work. Our analysis uses the empirical calibration for  $T_D$  in ULIRGs from Scoville et al. (2016) in which gas mass scales inversely with temperature. Scoville et al. (2016) advocates for a mass-weighted  $T_D$  of 25 K based largely on Herschel observations of nearby galaxies (Dunne et al. 2011; Dale et al. 2012; Auld et al. 2013). Other studies in ULIRGs (e.g. Sakamoto et al. 2021 and Walter et al. 2022) have shown that submm luminosity-weighted  $T_D$  can exceed 500 K in their nuclei. However, luminosity-weighted  $T_D$  are always higher than their mass-weighted counterparts for which the Scoville et al. (2016) relation is calibrated.

This unknown presents a challenge for the results of our continuum-based measurements. As is shown in the bottom panel of Figure 3, depending on the temperature assumption, the continuum-estimated molecular gas mass has a  $\sim 1.5$  dex range for each galaxy. At low  $T_D$ , at both comparison radii, the corresponding  $M_{\text{gas}}$  is driven *above* even the kinematic measurements from Medling et al. (2015). For III Zw

035 and IRAS F01364, the continuum-corrected  $M_{\text{enc}}$  is *below* the kinematic measurements. For the two galaxies with the highest luminosities, the continuum-corrected  $M_{\text{enc}}$  is *above* the kinematic measurements. This is consistent with the results of Scoville et al. (2016) for the two galaxies with the highest luminosities, which are III Zw 035 and IRAS F01364. The continuum-corrected  $M_{\text{enc}}$  is *below* the kinematic measurements for the two galaxies with the lowest luminosities, which are Medling et al. (2015) and Section 5. The continuum-corrected  $M_{\text{enc}}$  is *above* the kinematic measurements for the two galaxies with the intermediate luminosities, which are Medling et al. (2015) and Section 5.

035 this temperature is  $\sim$ 175 K and for IRAS F01364–1042 it is 19 K. If gas is the entirety of the  $M_{\text{enc}}$  in either case, it leaves no room for a SMBH or stellar component, so we consider these  $T_D$  values to be firm lower limits. As such, our continuum-based measurements are acting as an upper limit to the molecular gas mass content, and we must wait for more well-constrained  $T_D$  estimates for these galaxies to better understand the relationship between our measurement methods. CO excitation diagrams or radiative transfer modelling such as RADEX (van der Tak et al. 2007) at matched spatial scales with the assumption that the molecular gas and dust is well mixed (see Viti et al. 2014 for an example in NGC 1068) could lead to such results.

### 6.3. Implications for physics in nuclei of gas-rich mergers

Whether or not these black holes still remain overmassive with respect to scaling relations depends on which  $M_{\text{enc}}$  is correct. While there is evidence for an outflowing component in these systems, the physically cold gas with low turbulence is connected to dynamically cold kinematics. Because of the higher resolution of these ALMA CO data, we expect that the CO-derived  $M_{\text{enc}}$  are more reliable than previous estimates. In this case, the new enclosed masses calculated in Section 5 are upper limits on  $M_{\text{BH}}$ , and both  $M_{\text{enc}}$  and  $M_{\text{enc}} - M_{\text{gas}}$  fall along all scaling relations.

If we adopt values from Medling et al. (2015), those  $M_{\text{enc}}$  or  $M_{\text{enc}} - M_{\text{gas}}$  values all lie significantly above the scaling relations except for III Zw 035 when using a continuum-estimated  $M_{\text{gas}}$  with  $T_D \lesssim 175$  K. As was also found in Medling et al. (2019), kinematically-derived  $M_{\text{BH}}$  upper limits in ULIRGs may be significantly elevated due to the unresolved (gaseous) mass surrounding SMBH. The impact of cold gas contamination will depend on the nature of each individual system. In the case of the two LIRGs studied

here, the fraction of the  $M_{\text{BH}}$  estimates from Medling et al. (2015) that can be attributed to cold gas could be rather insignificant (1%) to very influential (75% or more depending on  $T_D$  and comparison value).

Evolutionarily for III Zw 035, IRAS F01364–1042, and NGC 6240N, overmassive SMBHs would suggest a model where black hole accretion occurs before growth on the larger galaxy scale. Simulations of this growth process suggest the opposite (Hopkins 2012; Cen 2012; Anglés-Alcázar et al. 2017). In merger-driven accretion, material has to travel to the nucleus, losing angular momentum along the way. On this path, there is expected to be a period of mixing and subsequent starburst that could cause global properties like  $\sigma_*$ ,  $L_{\text{bulge}}$ , and  $M_*$  to increase before the inflowing gas reaches the nucleus and accretes onto the SMBH. Other than gas accretion, BH-BH mergers can play a part in SMBH mass build-up. These events, however, have uncertain timescales and are not expected to contribute the majority of mass gain for SMBHs like ours (e.g. in Treister et al. 2012; Porras-Valverde et al. 2025). To explain a model where  $M_{\text{BH}}$  can outpace stellar growth in a merger, an angular momentum dissipation mechanism to facilitate rapid accretion of gas needs to be present.

The measurements presented here constrain  $M_{\text{BH}}$  corrections due to nuclear gas content to a lower limit. The current sample of four total nuclei (NGC6240 N/S, III Zw 035, and IRAS F01364–1042) is limited to these gas-rich mergers and is therefore still not representative or statistically large enough to make corrections to any general sample of SMBHs. In gas-rich LIRG mergers, at least a few to a few tens of percent of the  $\mathbf{r} \lesssim 77$  pc dynamically-measured  $M_{\text{enc}}$  could be molecular gas contaminating the  $M_{\text{BH}}$  measurements. Galaxy models should incorporate black hole mass and the full distribu-

tion of nuclear gas to properly simulate accretion physics.

Large nuclear gas reservoirs (as are shown to form in gas-rich mergers) are likely to form a viscous accretion disk. Viscous accretion disks transport mass much slower than predicted by Bondi-like accretion models, which are theoretically predicated on free-fall of gas onto the SMBH (Hoyle & Lyttleton 1939, Bondi & Hoyle 1944, Bondi 1952, Bisnovatyi-Kogan et al. 1979, Mayer et al. 2007, Power et al. 2011). We predict that models of gas-rich mergers that use a Bondi-like accretion prescription are overestimating accretion rates. Galactic nuclei can coalesce quicker than the larger scale disks, on timescales as short as 10 Myr (Khan et al. 2016).

## 7. CONCLUSIONS

In this work we used high resolution (sub-30 mas) CO(2-1) and continuum observations of two nearby LIRGs, III Zw 035 and IRAS F01364–1042, to measure molecular gas mass within the central few 10s of pc. Fractionally, we find that between 1 and 75% of the  $M_{\text{enc}}$  calculated in Medling et al. (2015) from stellar or gas kinematics can be attributed to molecular gas within 10s of parsecs from the central black holes. At higher resolution, the  $M_{\text{enc}}$  within the inner 40 mas are 91–93% lower than from kinematics taken over a larger region. Molecular gas mass contributes at least 15% of the new  $M_{\text{enc}}$ .

Because of the higher resolution and less kinematically disturbed nature of cold gas, we expect the new dynamically-derived  $M_{\text{enc}}$  calculated in Section 5 to be closer to the true  $M_{\text{BH}}$  of these merging systems. In all cases, starting from this  $M_{\text{enc}}$  III Zw 035 and IRAS F01364–1042 fall on the  $M_{\text{BH}}$  scaling relations shown in Figure 6. In most cases this is true even before subtracting the enclosed molecular gas mass. These new measurements are still limited in that they are enclosed masses rather than black hole masses, and our sample size is low. Very high resolution observations of cold

gas for the remaining sample of overmassive black holes found in Medling et al. (2015) (IRAS F17207-0014, NGC 2623, and CGCG 436-030) and independent  $M_{\text{enc}}$  measurements of NGC 6240’s nuclei would allow us to understand if these nuclei **are all consistent with** scaling relations when using cold gas as a tracer.

The accuracy of accretion modeling is directly limited by our understanding of typical nuclear gas masses and distributions. With significant nuclear molecular gas, a viscous accretion disk is likely to form, causing a slower rate of accretion. However, the resulting non-spherical accretion could potentially circumvent the Eddington limit; if super-Eddington accretion were common, it would have significant implications for the growth of supermassive black holes in the early universe and throughout cosmic time. Many cosmological simulations rely on spherically-symmetric black hole accretion rate prescriptions to predict the impacts of black hole growth and subsequent AGN feedback. The presence of nuclear gas disks could limit the power of such predictions.

Our current sample of four nuclei (NGC6240 N/S, III Zw 035, and IRAS F01364–1042) is not large enough nor representative of all gas-rich mergers – we need more high resolution datasets to push towards a unified picture of nuclear gas mass within galactic nuclei. Regardless, gas should not be left unconsidered when using dynamics to derive  $M_{\text{BH}}$  in gas-rich galaxies.

## 8. ACKNOWLEDGEMENTS

The authors thank first the indigenous people of Hawai‘i for the opportunity to be guests on your sacred mountain. We recognize the cultural significance that Maunakea holds for your community and are privileged to use data borne from science conducted in such a setting. We wish to pay respect to the Atacameño community of the Chajnantor Plateau, whose tradition

tional home now also includes the ALMA observatory.

We would like to thank the anonymous reviewer for their contributions to this project, in particular with regards to our independent upper limit on  $M_{\text{BH}}$ . This work makes use of the following data from ALMA: projects 2018.1.01123.S and 2019.1.00811.S (PI: Medling); project 2017.1.01235.S (PI: Barcos-Muñoz). ALMA is a partnership of ESO (representing its member states), NSF (USA) and NINS (Japan), together with NRC (Canada) and NSC and ASIAA (Taiwan) and KASI (Republic of Korea), in cooperation with the Republic of Chile. The Joint ALMA Observatory is operated by ESO, AUI/NRAO and NAOJ. The National Radio Astronomy Observatory is a facility of the National Science Foundation operated under cooperative agreement by Associated Universities, Inc. Some of the data presented herein were obtained at the W. M. Keck Observatory, which is operated as a scientific partnership among the California Institute of Technology, the University of California and the National Aeronautics and Space Administration. The Observatory was made possible by the generous financial support of the W. M. Keck Foundation. The authors also wish to thank the W.M. Keck Observatory staff for their efforts on the OSIRIS+AO instrumentation. JA thanks the staff at NRAO Charlottesville for their generous mentorship during invaluable in-person visits and their assistance virtually. JA also thanks Enrico di Teodoro for his input on final model fits. JA acknowledges support from NRAO Student Observing Support program awards SOSPA7-017 and SOSPADA-017. JA and AMM also acknowledge support from NSF CAREER number 2239807. JA, AMM, and VU acknowledge partial funding support from the NASA Astrophysics Data Analysis Program (ADAP) grant number 80NSSC23K0750. VU further acknowledges

partial funding support from NASA Astrophysics Data Analysis Program (ADAP) grant number 80NSSC20K0450, Space Telescope Science Institute grants, numbers HST-AR-17063.005-A, HST-GO-17285.001, and JWST-GO-01717.001. CC acknowledges funding from the European Union’s Horizon Europe research and innovation programme under grant agreement No. 101188037 (AtLAST2). Some of the data presented in this article was obtained from the Mikulski Archive for Space Telescopes (MAST) at the Space Telescope Science Institute. The specific observations analyzed can be accessed via <https://doi.org/10.17909/h5ts-qy16>. JM is funded by the Hirsch Foundation. CR acknowledges support from the Fondecyt Iniciacion grant 11190831 and ANID BASAL project FB210003. The Flatiron Institute is supported by the Simons Foundation. CR acknowledges support from Fondecyt Regular grant 1230345 and ANID BASAL project FB210003.

*Software:* Astropy (Astropy Collaboration et al. 2013, 2018, 2022), Matplotlib (Hunter 2007), NumPy (Harris et al. 2020), CASA (CASA Team et al. 2022), and <sup>3D</sup>Barolo (Di Teodoro & Fraternali 2015).

## REFERENCES

Anglés-Alcázar, D., Faucher-Giguère, C.-A., Quataert, E., Hopkins, P. F., Feldmann, R., Torrey, P., Wetzel, A., & Kereš, D. 2017, MNRAS, 472, L109

Armus, L., et al. 2009, PASP, 121, 559

Astropy Collaboration et al. 2013, A&A, 558, A33

—. 2018, AJ, 156, 123

—. 2022, ApJ, 935, 167

Auld, R., et al. 2013, MNRAS, 428, 1880

Barcos-Muñoz, L., et al. 2017, ApJ, 843, 117

Barth, A. J., Strigari, L. E., Bentz, M. C., Greene, J. E., & Ho, L. C. 2009, ApJ, 690, 1031

Beifiori, A., Courteau, S., Corsini, E. M., & Zhu, Y. 2012, MNRAS, 419, 2497

Bennert, V. N., Auger, M. W., Treu, T., Woo, J.-H., & Malkan, M. A. 2011, ApJ, 742, 107

Bennert, V. N., et al. 2021, ApJ, 921, 36

Bentz, M. C., et al. 2013, ApJ, 767, 149

Bisnovatyi-Kogan, G. S., Kazhdan, Y. M., Klypin, A. A., Lutskii, A. E., & Shakura, N. I. 1979, Soviet Ast., 23, 201

Bolatto, A. D., Wolfire, M., & Leroy, A. K. 2013, ARA&A, 51, 207

Bondi, H. 1952, MNRAS, 112, 195

Bondi, H., & Hoyle, F. 1944, MNRAS, 104, 273

Briggs, D. S. 1995, in American Astronomical Society Meeting Abstracts, Vol. 187, American Astronomical Society Meeting Abstracts, 112.02

Burton, W. B., Gordon, M. A., Bania, T. M., & Lockman, F. J. 1975, ApJ, 202, 30

Cackett, E. M., Bentz, M. C., & Kara, E. 2021, iScience, 24, 102557

Cappellari, M. 2008, MNRAS, 390, 71

CASA Team et al. 2022, PASP, 134, 114501

Cen, R. 2012, ApJ, 755, 28

Ciccone, C., et al. 2018, ApJ, 863, 143

Cisternas, M., et al. 2011, ApJL, 741, L11

Clavel, J., et al. 1991, ApJ, 366, 64

Combes, F. 1991, ARA&A, 29, 195

Comrie, A., et al. 2021, CARTA: The Cube Analysis and Rendering Tool for Astronomy

Condon, J. J., & Ransom, S. M. 2016, Essential Radio Astronomy

Cortes, P. A., et al. 2023, ALMA Cycle 10 Technical Handbook (Cycle 10; Doc. 10.3; version 1.1), Zenodo. <https://doi.org/10.5281/zenodo.7822943>

Cretton, N., de Zeeuw, P. T., van der Marel, R. P., & Rix, H.-W. 1999, ApJS, 124, 383

Dale, D. A., et al. 2012, ApJ, 745, 95

Davies, R., et al. 2024, A&A, 689, A263

Davis, B. L., Graham, A. W., & Cameron, E. 2018, ApJ, 869, 113

—. 2019, ApJ, 873, 85

Di Teodoro, E. M., & Fraternali, F. 2015, MNRAS, 451, 3021

Diaz Trigo, M., Carpenter, J., Maude, L., Miura, R., & Plunkett, A. 2019, ALMA Cycle 7 Proposer's Guide, 2019, ALMA Cycle 7 Proposer's Guide, ALMA Doc. 7.2 v1.0 : Proposer's guide for the Atacama Large Millimeter/Submillimeter Array (ALMA) Cycle 7, Doc. 7.2, ver. 1.0, 2019

Dickman, R. L. 1978, ApJS, 37, 407

Dunne, L., et al. 2011, MNRAS, 417, 1510

Event Horizon Telescope Collaboration et al. 2019, ApJL, 875, L1

Faber, S. M., & Jackson, R. E. 1976, ApJ, 204, 668

García-Burillo, S., et al. 2021, A&A, 652, A98

Gebhardt, K., et al. 2000, ApJL, 539, L13

Genzel, R., Eisenhauer, F., & Gillessen, S. 2010, Reviews of Modern Physics, 82, 3121

Ghez, A. M., et al. 2008, ApJ, 689, 1044

Gültekin, K., et al. 2009, ApJ, 698, 198

Häring, N., & Rix, H.-W. 2004, ApJL, 604, L89

Harris, C. R., et al. 2020, Nature, 585, 357

Heckman, T. M., & Best, P. N. 2014, ARA&A, 52, 589

Herrero-Illana, R., et al. 2019, A&A, 628, A71

Hinshaw, G., et al. 2009, ApJS, 180, 225

Ho, L. 1999, in Astrophysics and Space Science Library, Vol. 234, Observational Evidence for the Black Holes in the Universe, ed. S. K. Chakrabarti, 157

Hopkins, P. F. 2012, MNRAS, 420, L8

Hopkins, P. F., Cox, T. J., Kereš, D., & Hernquist, L. 2008a, ApJS, 175, 390

Hopkins, P. F., Hernquist, L., Cox, T. J., & Kereš, D. 2008b, ApJS, 175, 356

Horne, K., Peterson, B. M., Collier, S. J., & Netzer, H. 2004, PASP, 116, 465

Hoyle, F., & Lyttleton, R. A. 1939, Proceedings of the Cambridge Philosophical Society, 35, 405

Hunter, J. D. 2007, Computing in Science & Engineering, 9, 90

Khan, F. M., Fiacconi, D., Mayer, L., Berczik, P., & Just, A. 2016, *ApJ*, 828, 73

Kormendy, J. 1993, in *The Nearest Active Galaxies*, ed. J. Beckman, L. Colina, & H. Netzer, 197–218

Kormendy, J., & Gebhardt, K. 2001, in *American Institute of Physics Conference Series*, Vol. 586, 20th Texas Symposium on relativistic astrophysics, ed. J. C. Wheeler & H. Martel, 363–381

Kormendy, J., & Ho, L. C. 2013, *ARA&A*, 51, 511

Kormendy, J., et al. 1997, *ApJL*, 482, L139

Lauer, T. R., et al. 1995, *AJ*, 110, 2622

Lutz, D., et al. 2020, *A&A*, 633, A134

Magorrian, J., et al. 1998, *AJ*, 115, 2285

Marconi, A., & Hunt, L. K. 2003, *ApJL*, 589, L21

Mayer, L., Kazantzidis, S., Madau, P., Colpi, M., Quinn, T., & Wadsley, J. 2007, *Science*, 316, 1874

McConnell, N. J., & Ma, C.-P. 2013, *ApJ*, 764, 184

McLure, R. J., & Dunlop, J. S. 2002, *MNRAS*, 331, 795

Medling, A. M., Ammons, S. M., Max, C. E., Davies, R. I., Engel, H., & Canalizo, G. 2011, *ApJ*, 743, 32

Medling, A. M., et al. 2014, *ApJ*, 784, 70

—. 2015, *ApJ*, 803, 61

—. 2019, *ApJL*, 885, L21

Merritt, D., & Ferrarese, L. 2001, *MNRAS*, 320, L30

Mirabel, I. F., & Sanders, D. B. 1988, *ApJ*, 335, 104

Montoya Arroyave, I., et al. 2023, *A&A*, 673, A13

Morgan, C. W., Kochanek, C. S., Morgan, N. D., & Falco, E. E. 2010, *ApJ*, 712, 1129

Partridge, B., López-Caniego, M., Perley, R. A., Stevens, J., Butler, B. J., Rocha, G., Walter, B., & Zacc hei, A. 2016, *ApJ*, 821, 61

Pihlström, Y. M., Conway, J. E., Booth, R. S., Diamond, P. J., & Polatidis, A. G. 2001, *A&A*, 377, 413

Planck Collaboration et al. 2016, *A&A*, 596, A104

Porras-Valverde, A. J., Ricarte, A., Natarajan, P., Somerville, R. S., Gabrielpillai, A., & Yung, L. Y. A. 2025, arXiv e-prints, arXiv:2504.11566

Power, C., Nayakshin, S., & King, A. 2011, *MNRAS*, 412, 269

Sakamoto, K., Martín, S., Wilner, D. J., Aalto, S., Evans, A. S., & Harada, N. 2021, *ApJ*, 923, 240

Sanders, D. B., & Mirabel, I. F. 1996, *ARA&A*, 34, 749

Sandstrom, K. M., et al. 2013, *ApJ*, 777, 5

Schwarzschild, M. 1979, *ApJ*, 232, 236

Scoville, N., et al. 2015, *ApJ*, 800, 70

—. 2016, *ApJ*, 820, 83

Scoville, N. Z., & Solomon, P. M. 1975, *ApJL*, 199, L105

Silk, J., & Rees, M. J. 1998, *A&A*, 331, L1

Solomon, P. M., Scoville, N. Z., Penzias, A. A., Wilson, R. W., & Jefferts, K. B. 1972, *ApJ*, 178, 125

Solomon, P. M., & Vanden Bout, P. A. 2005, *ARA&A*, 43, 677

Stierwalt, S., et al. 2013, *ApJS*, 206, 1

Teng, Y.-H., et al. 2022, *ApJ*, 925, 72

Treister, E., Schawinski, K., Urry, C. M., & Simmons, B. D. 2012, *ApJL*, 758, L39

Tremaine, S., et al. 2002, *ApJ*, 574, 740

U, V., et al. 2012, *ApJS*, 203, 9

—. 2013, *ApJ*, 775, 115

—. 2019, *ApJ*, 871, 166

—. 2022, *ApJ*, 925, 52

van den Bosch, R. C. E., van de Ven, G., Verolme, E. K., Cappellari, M., & de Zeeuw, P. T. 2008, *MNRAS*, 385, 647

van der Tak, F. F. S., Black, J. H., Schöier, F. L., Jansen, D. J., & van Dishoeck, E. F. 2007, *A&A*, 468, 627

Vestergaard, M., & Peterson, B. M. 2006a, *ApJ*, 641, 689

—. 2006b, *ApJ*, 641, 689

Viti, S., et al. 2014, *A&A*, 570, A28

Walsh, J. L., van den Bosch, R. C. E., Barth, A. J., & Sarzi, M. 2012, *ApJ*, 753, 79

Walter, F., et al. 2022, *ApJ*, 927, 21

Wang, J., Zhang, Z., & Shi, Y. 2011, *MNRAS*, 416, L21

Wilson, W. J., Schwartz, P. R., Epstein, E. E., Johnson, W. A., Etcheverry, R. D., Mori, T. T., Berry, G. G., & Dyson, H. B. 1974, *ApJ*, 191, 357

Wright, E. L. 2006, *PASP*, 118, 1711

Yoon, I. 2017, *MNRAS*, 466, 1987

## APPENDIX

## A. KINEMATIC MODELING

This section of the Appendix describes additional detail about the <sup>3D</sup>Barolo tilted-ring modeling used in this work to calculate  $M_{\text{enc}}$  from the cold CO gas. <sup>3D</sup>Barolo is a tilted-ring modeling algorithm with a task called **3DFIT**. This algorithm takes in data with kinematic information, and derives rotational velocities for tilted rings spaced at intervals specified by the user. For our purposes with the high resolution CO(2-1) cubes, we use **3DFIT** in two-stage mode. In two-stage mode **3DFIT** regularizes the input parameters, then enters a second fitting phase (Di Teodoro & Fraternali 2015).

We tested different methods of building the **3DFIT** mask (used by the program to determine where there is genuine emission), using both **SEARCH** and **SMOOTH&SEARCH**, and we tested different input parameters (e.g. PA, inclination, redshift, and systemic velocity). In testing, as is suggested by the authors of <sup>3D</sup>Barolo, we judge model goodness by examining the line intensity maps and PV plots (as in Figure 5). Models and residuals produced in this way are shown in Figures 7 and 8, and output tilted-ring parameters can be found in Table 4. We use the resulting rotational velocities in Section 5 to calculate  $M_{\text{enc}}$ .

Galaxy	R (arcsec)	$v_{\text{rot}}$ (km s <sup>-1</sup> )	$\sigma_v$ (km s <sup>-1</sup> )	P.A. (deg)
III Zw 035	0.010	117.299 <sup>+15.688</sup> <sub>-16.559</sub>	12.962 <sup>+13.157</sup> <sub>-13.157</sub>	19.765
	0.030	116.632 <sup>+24.541</sup> <sub>-23.268</sub>	70.446 <sup>+13.758</sup> <sub>-13.758</sub>	19.765
	0.050	127.537 <sup>+17.974</sup> <sub>-15.995</sub>	71.341 <sup>+13.321</sup> <sub>-11.454</sub>	19.765
	0.070	138.887 <sup>+14.576</sup> <sub>-13.268</sub>	64.466 <sup>+11.887</sup> <sub>-9.568</sub>	19.765
	0.090	155.569 <sup>+13.731</sup> <sub>-15.584</sub>	66.102 <sup>+11.342</sup> <sub>-12.737</sub>	19.765
	0.110	174.523 <sup>+20.043</sup> <sub>-21.25</sub>	67.762 <sup>+14.458</sup> <sub>-14.458</sub>	19.765
	0.130	184.272 <sup>+19.313</sup> <sub>-19.348</sub>	58.828 <sup>+12.395</sup> <sub>-12.395</sub>	19.765
	0.150	195.405 <sup>+21.794</sup> <sub>-22.034</sub>	60.046 <sup>+12.700</sup> <sub>-12.700</sub>	19.765
	0.170	206.447 <sup>+24.747</sup> <sub>-26.912</sub>	56.457 <sup>+12.373</sup> <sub>-13.456</sub>	19.765
	0.190	210.448 <sup>+28.939</sup> <sub>-26.236</sub>	44.030 <sup>+14.469</sup> <sub>-13.118</sub>	19.765
IRAS F01364–1042	0.013	158.335 <sup>+21.370</sup> <sub>-17.959</sub>	30.945 <sup>+11.350</sup> <sub>-11.103</sub>	240.958
	0.039	150.972 <sup>+18.810</sup> <sub>-22.804</sub>	65.695 <sup>+14.215</sup> <sub>-14.215</sub>	236.849
	0.065	162.998 <sup>+13.971</sup> <sub>-14.571</sub>	61.799 <sup>+9.680</sup> <sub>-9.638</sub>	227.546
	0.091	173.123 <sup>+13.000</sup> <sub>-12.731</sub>	62.743 <sup>+8.393</sup> <sub>-8.159</sub>	223.659
	0.117	182.589 <sup>+11.929</sup> <sub>-13.586</sub>	63.689 <sup>+8.303</sup> <sub>-9.952</sub>	224.687
	0.143	180.143 <sup>+15.618</sup> <sub>-15.427</sub>	64.256 <sup>+10.198</sup> <sub>-10.775</sub>	227.474
	0.169	168.557 <sup>+18.185</sup> <sub>-18.222</sub>	61.354 <sup>+10.996</sup> <sub>-11.841</sub>	229.847
	0.195	152.269 <sup>+22.261</sup> <sub>-20.124</sub>	57.424 <sup>+12.634</sup> <sub>-13.882</sub>	231.254
	0.221	133.305 <sup>+23.109</sup> <sub>-22.004</sub>	53.216 <sup>+11.214</sup> <sub>-11.214</sub>	232.371
	0.247	137.034 <sup>+23.665</sup> <sub>-26.155</sub>	45.981 <sup>+12.003</sup> <sub>-12.003</sub>	235.257

**Table 4.** <sup>3D</sup>Barolo phase two best-fit tilted-ring model parameters for III Zw 035 and IRAS F01364–1042. The velocity dispersion modeling (column 4) may be somewhat elevated due to contamination of the CO line profiles by an outflowing component. The second and third columns, tilted-ring radius and rotational velocity, are used to compute  $M_{\text{enc}}$  as found in Section 5. The inclination angles for both galaxies were constant as a function of radius: 75 and 61 degrees for III Zw 035 and IRAS F01364–1042 respectively. Position angle (column 5), while constant for III Zw 035, was fit as a free variable for both galaxies.

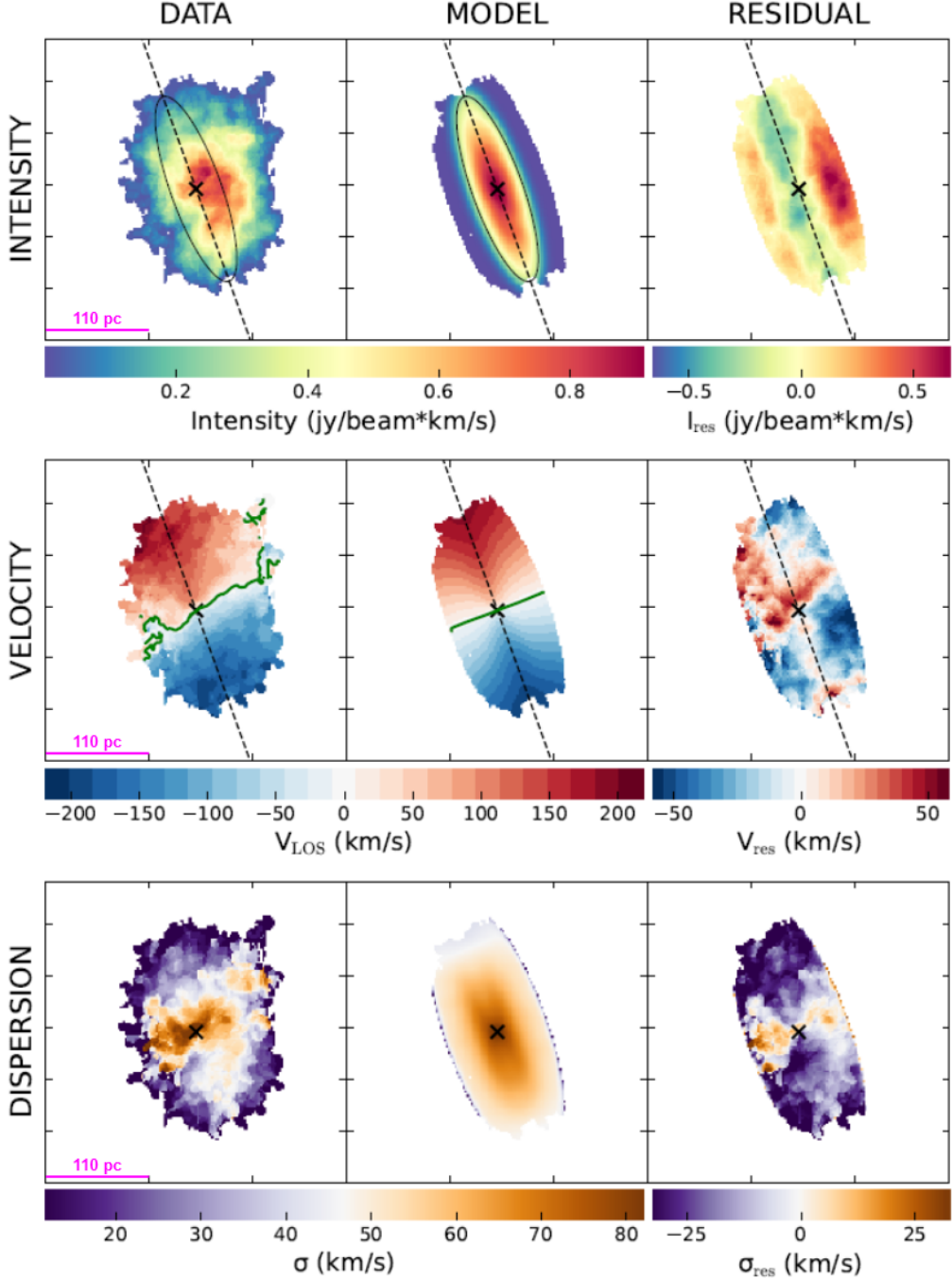


**Figure 7.** III Zw 035 ring models produced by <sup>3D</sup>Barolo, used to calculate  $M_{\text{enc}}$  in Section 5. Input CO(2-1) images are the same as presented in Figure 2 ( $33 \times 28$  mas beam size), and input parameters include PA, inclination, redshift, and systemic velocity. Ring model output parameters can be found in Table 4. Green lines in the first two velocity panels indicate  $0 \text{ km s}^{-1}$  with respect to the galaxy's systemic velocity, which indicate potential disk-warping. The higher velocity dispersion residuals of the III Zw 035 disk along its minor axis likely reflect broadening of the CO line profile by the molecular outflow.

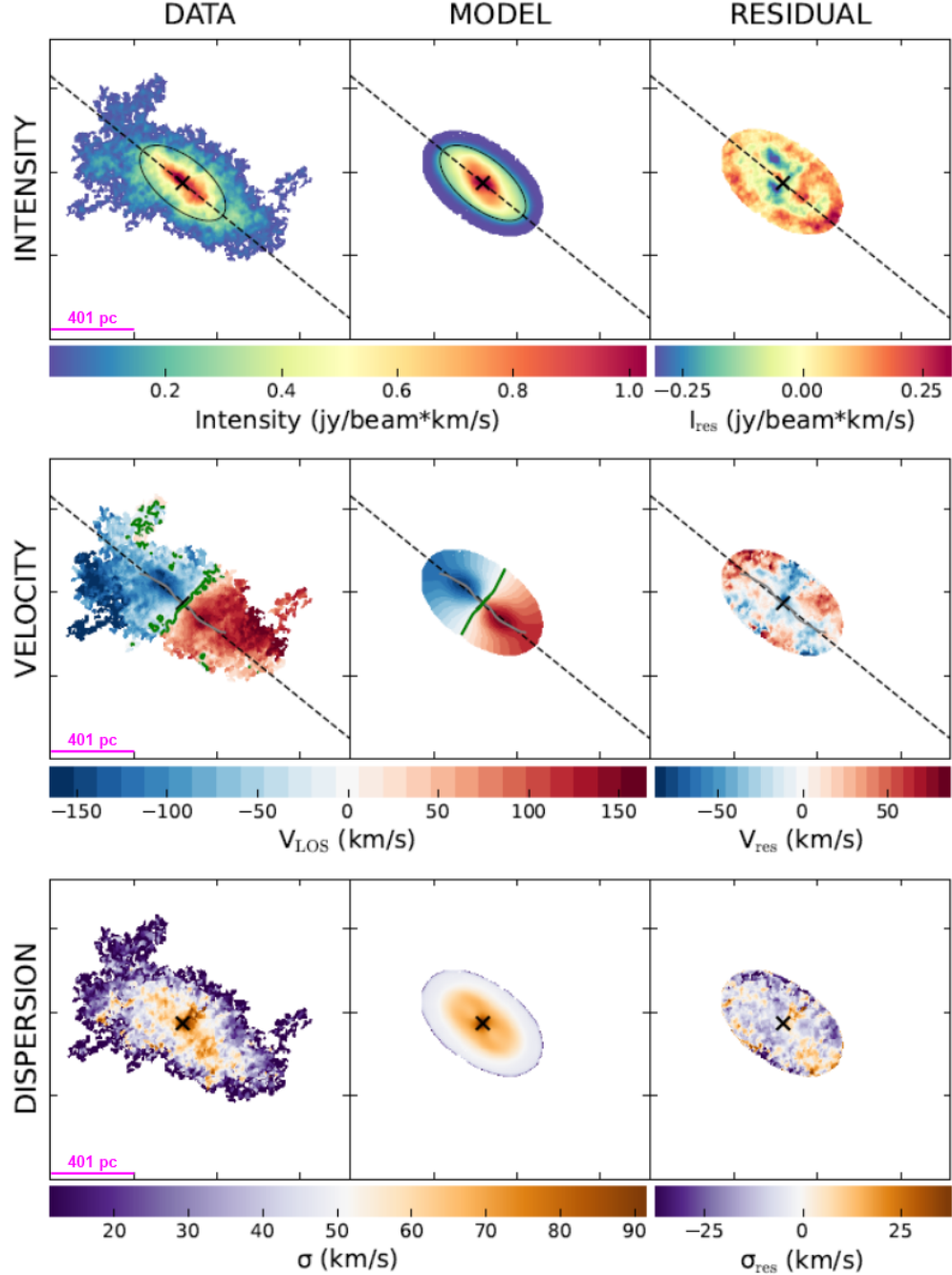


**Figure 8.** IRAS F01364–1042 ring models produced by  ${}^3\text{D}\text{Barolo}$ , used to calculate  $M_{\text{enc}}$  in Section 5. Input CO(2-1) images are the same as presented in Figure 2 (42  $\times$  39 mas beam size), and input parameters include PA, inclination, redshift, and systemic velocity. Ring model output parameters can be found in Table 4. Green lines in the first two velocity panels indicate  $0 \text{ km s}^{-1}$  with respect to the galaxy’s systemic velocity. IRAS F01364–1042 is particularly well-defined by a rotating disk, although residuals show some evidence of outflows along the minor axis in velocity space.